applied optics

THz coherent lensless imaging

Lorenzo Valzania,[1,2,*,†] Yuchen Zhao,[3,†] Lu Rong,[4,5] Dayong Wang,[4,5] Marc Georges,[3] Erwin Hack,[1] and Peter Zolliker[1]

[1]Laboratory for Transport at Nanoscale Interfaces, Empa, Swiss Federal Laboratories for Materials Science and Technology, 129 Uberlandstrasse, Dubendorf 8600, Switzerland
[2]Currently with the Laboratoire Kastler Brossel, Sorbonne Université, École Normale Supérieure—Paris Sciences et Lettres (PSL) Research University, CNRS, Collège de France, 24 rue Lhomond, Paris 75005, France
[3]Centre Spatial de Liège, STAR Research Unit—Université de Liège, Liège Science Park, Avenue du Pré Aily, Angleur 4031, Belgium
[4]College of Applied Sciences, Beijing University of Technology, 100 Ping Le Yuan, Beijing 100124, China
[5]Beijing Engineering Research Center of Precision Measurement Technology and Instruments, 100 Ping Le Yuan, Beijing 100124, China
*Corresponding author: lorenzo.valzania@empa.ch

Received 22 July 2019; revised 26 September 2019; accepted 28 September 2019; posted 1 October 2019 (Doc. ID 373049); published 7 November 2019

Imaging with THz radiation has proved an important tool for both fundamental science and industrial use. Here we review a class of THz imaging implementations, named coherent lensless imaging, that reconstruct the coherent response of arbitrary samples with a minimized experimental setup based only on a coherent source and a camera. After discussing the appropriate sources and detectors to perform them, we detail the fundamental principles and implementations of THz digital holography and phase retrieval. These techniques owe a lot to imaging with different wavelengths, yet innovative concepts are also being developed in the THz range and are ready to be applied in other spectral ranges. This makes our review useful for both the THz and imaging communities, and we hope it will foster their interaction. © 2019 Optical Society of America

https://doi.org/10.1364/AO.58.00G256 Provided under the terms of the OSA Open Access Publishing Agreement

1. INTRODUCTION

Terahertz (THz) radiation denotes the portion of the electromagnetic spectrum whose frequency ranges from 0.1 THz to 10 THz, lying between the infrared and microwave regions [1]. As such, its interaction with matter shares properties of both neighboring bands. Like microwaves, THz waves can penetrate insulating materials, such as building and plastic materials [2–5], intrinsic semiconductors [6], paper [7], and fabrics [8]. Owing to the shorter wavelength compared to microwaves, THz waves offer a higher spatial resolution, paving the way for new non-destructive tools for industrial inspection with sub-mm resolution [9]. Like the infrared band, the THz band is host to a wide variety of energy transitions in aqueous [10] and solid-state systems [11], making THz radiation a valuable probe to investigate fundamental properties of matter, as well.

In order to fully exploit this potential, it is crucial to develop imaging techniques using THz radiation. Research on THz imaging has been growing for more than 20 years [12,13], and its advances go hand in hand with the improvement of THz sources and detectors.

In particular, ultrafast lasers enabled the development of broadband THz sources and coherent detectors [14]. Along these lines, imaging with THz time-domain spectroscopy (THz-TDS) [15] has found widespread use in both industrial [16] and scientific applications [17,18]. In the latter case, it is worth mentioning its use in near-field setups breaking the diffraction limit [19,20]. The most important advantage of imaging with THz-TDS is its ultrafast detection, which allows direct measurement of the time evolution of the THz electric field, so that the complex refractive index of the object can be extracted [21]. This comes at the expense of the flexibility of the setup, which should always feature synchronization between source and detector. Furthermore, manufacturing detector arrays with usable size for full-field imaging is currently prevented by the need for high-power (Watt-level) femtosecond lasers, thus limiting THz-TDS imaging as a scanning technique [22,23]. The use of THz-TDS towards real-time imaging has been recently reviewed by Guerboukha *et al.* [13].

Other THz imaging techniques borrowed their operational principle from techniques implemented at shorter wavelengths, from the visible to the x-ray range. THz tomographic techniques are a valuable solution to obtain non-destructive three-dimensional (3D) reconstructions of weakly absorbing samples [24], either from projections taken at different angular positions [25] or in a confocal microscopy arrangement in reflection mode [26], where in both implementations, the acquisition can be made coherent with the addition of a reference arm. Compressive sensing is a smart computational imaging concept, where the beam transmitted through the

object is modulated with a carefully designed mask, and the resulting intensity is recorded with a single-pixel detector. Provided that the object transmission function or its gradient is sparse, its reconstruction is allowed from a number of measurements lower than the number of unknown pixels [27]. First demonstrated with a THz source by Chan *et al.* [28,29], it represents a cheaper alternative to imaging techniques using THz cameras, although it imposes stringent requirements on the object transmission function.

Imaging techniques delivering coherent reconstructions of arbitrary objects, with flexible and compact setups and using cameras, belong to the realm of coherent lensless imaging (see, e.g., [30]). The fact that cameras are not fast enough to record both the amplitude and phase of the electric field impinging on them leads to the so-called "phase problem," which entails extracting the missing phase information from intensity-only measurements. Upon illuminating the object with a spatially and temporally coherent beam, coherent lensless imaging techniques solve the phase problem using one or more diffraction patterns of the object (with iterative algorithms referred to as "phase retrieval" [31,32]), or their interference with a known reference wavefront (holographic techniques [33]). Because they obviate the need for imaging components such as lenses, coherent lensless imaging techniques were originally conceived for x-ray and electron imaging, where the quality of optics used to be poor. Nevertheless, this makes them particularly useful in THz imaging too, where the dramatic increase in wavelength would require optics so large as to make conventional imaging experiments more difficult and unpractical to implement. As a rule of thumb given in [34], the aperture of the optics should be at least twice that of the incoming beam size in order to avoid diffraction effects.

In this contribution, THz coherent lensless imaging techniques will be reviewed, with a two-fold relevance. First, its content will complement the two latest reviews of THz imaging [12,13], mostly focusing on THz-TDS imaging, near-field imaging, tomography, and compressive sensing. Second, we have realized that the peculiar interaction of THz radiation with materials triggered the development of new THz coherent lensless imaging techniques, which can in turn be implemented at different wavelengths [35,36]. This review is therefore meant to build a bridge between the THz and imaging communities, both of which are expected to benefit from it.

The paper summarizes both the technical and theoretical aspects of THz coherent lensless imaging. Section 2 reviews the coherent THz sources and detectors used to perform them, and lists the source–detector combinations that yielded successful THz imaging setups. Section 3 explains the operational principles of digital holographic and phase retrieval techniques and reports on their implementation with THz radiation. Finally, a summary and outlook are provided in Section 4.

2. COHERENT THz SOURCES AND DETECTORS

A. Overview

The generation and detection of THz radiation remain the most challenging yet revolutionary domains (see, e.g., [1,13,37–40]). In particular, coherent THz sources and intensity-sensitive detectors are the core elements employed in THz coherent imaging systems. This section discusses the representative THz sources and detectors with emphasis on their applicability in THz coherent lensless imaging systems.

B. Coherent THz Sources

The mechanisms for coherent THz generation are based on various physical principles [1]. As the THz range is located between microwaves and infrared radiation, it is no surprise that THz radiation can be generated by both optical and electronic techniques. In the following, we discuss the THz sources by their generation principle, from pure optical to pure electronic.

Gas lasers pumped by a CO_2 laser are a high-power table-top source of continuous-wave (CW) THz radiation. They are based on stimulated emission from rotational transitions in molecules such as methanol, formic acid, and their deuterated compounds and offer a wide selection of single-line emissions from around 60 μm to 500 μm with powers up to several tens of mW [41]; CW radiation at 2.52 THz (118.8 μm) can exceed 150 mW [42]. The single-line operation with a coherence length of several meters and the power level make them a convenient source for coherent imaging (see Section 2.4).

Difference frequency generation (DFG) provides a tunable THz source by mixing two lasers in a non-linear medium [43–45] and operates at room temperature. Because of the non-linear optical principle, DFG is preferably based on pulsed lasers. In optical rectification second-order non-linearity is used to generate a difference frequency in the THz domain. Here, the use of pulsed lasers limits the coherence length to typically below a few mm [46]. In four-wave mixing, third-order non-linearity is used from non-linear crystals [47], but also from water vapor or laser-induced air plasma [48]. THz sources based on DFG have not been used so far for coherent imaging. For CW photomixing, powers of a few 10 μW and a coherence length of 13 m were reported [44], limited by the coherence length of the pump lasers. As the optical path rather than a CW phase is measured, pulsed sources are applicable for coherent imaging only when used in scanning mode.

Photoconductive antennas are used to generate a burst of THz radiation. These combined electronic–optical devices use photoinduced currents from micro-antennas [49] or photomixing of two lasers/laser modes in a semiconductor coupled to microstructured antennas [50], generating a ps THz pulse corresponding to a pulse length of 300 μm or to a spectral band spanning typically 0.1 THz to 7 THz. To obtain phase information, a synchronized gated detection device is used.

Quantum cascade Lasers (QCLs) are electrically pumped unipolar lasers based on electronic transitions from semiconductor multilayered structures [51–53]. QCLs are attractive for coherent imaging, because they are table-top and approach powers of a fraction of a W [54]. Although Stirling, liquid nitrogen, or cryogenic cooling would increase the output power [55,56], progress is being made towards room-temperature high-power sources [57,58]. There exist single-line and multi-line devices operating in pulsed mode, providing a CW equivalent THz power of several mW [59]. The coherence length of a single-line QCL is typically several meters [60] and can reach several hundred meters with external stabilization [61].

p-type Ge-lasers [62] are tunable CW THz sources, but need cryogenic cooling to helium temperature and are not practical for coherent THz imaging.

Electronic solid-state oscillators are also based on semiconductor technologies [63]. Impact ionization avalanche transit-time (IMPATT) diodes and Gunn diodes are compact sources in this category. A microwave oscillator is created by applying a DC voltage to bias the device into its negative resistance region. Gunn diodes based on gallium arsenide are made for frequencies up to 200 GHz, while those relying on gallium nitride can reach up to 3 THz [64,65]. As these devices operate at room temperature in CW mode emitting monochromatic radiation in the range of 0.1–1 THz (from here on referred to as "sub-THz radiation"), they are suitable sources for coherent imaging.

Frequency multiplier chains are often used with electronic sources such as Gunn and IMPATT diodes to generate even higher frequency radiation. Frequency multipliers are Schottky-diode-based or transistor-based electronic circuits, which have a nonlinear response to electromagnetic waves [65]. They generate higher harmonic components of the incoming wave. With a suitable filter or waveguide, harmonics are collected. It is also possible to use several frequency multipliers in series to produce even higher frequencies. Frequency multiplier modules are often integrated in the transmitter and receiver parts of a millimeter wave vector network analyzer (VNA) as a frequency extender.

Backward wave oscillators (BWOs) are vacuum tubes used to generate microwaves up to the THz range. Belonging to the traveling-wave tube family, they are oscillators tunable over a wide range of frequencies by varying the accelerating voltage [66,67]. The output power in the range of 1 mW at 1 THz to 50 mW at 0.2 THz is coupled out near the electron gun. Despite lower power at high frequencies, a combination of millimeter-wave BWO (100–370 GHz) with frequency multipliers offers a very attractive alternative to sub-mm wave BWO, extending their spectral coverage to 2.2 THz [68]. High output powers, narrow spectral linewidths, and frequency tunability are the main advantages of these THz sources. Due to the good quality wavefront they produce, they find use as illuminators in coherent THz imaging [69].

THz sources based on free electron lasers (FELs) are emerging. In an early work investigating the possibility of THz 3D holographic tomography, a coherence length of 1 cm for the THz pulse was reported [70]. The FEL output pulse is typically near-Fourier-transform limited. A discussion of high-power THz sources based on vacuum electronics, including BWO and FEL, is found in [71].

C. THz Detectors

Imaging with array detectors working up to video frame rates allows dynamic measurements and is today the method of choice for THz coherent lensless imaging. The first approaches to THz hologram recording using array detectors were discussed already in 2005 [72–74]. One of them uses indirect thermal methods to record the temperature increase of a plate induced by absorption of THz radiation. This is based on thermography cameras or on thermally sensitive phosphor plates, which are read out with a CCD camera [75]. Triggered by a first study conducted at the U.S. Naval Research Lab (NRL) [14], uncooled micro-bolometer arrays for thermal imaging started to be used in the THz range [76–78]. A comprehensive and quite recent compilation of available THz detectors is given in the review paper by Dhillon *et al.* [1].

In the following, we summarize the properties of different detector types that have been utilized in lensless imaging.

Pyroelectric cameras are solid-state arrays able to detect radiation spanning from infrared to THz using $LiTaO_3$ pyroelectric crystals as detector material. A chopper is integrated to modulate the irradiance in time. Pyrocam III and Pyrocam IV are commercially available pyroelectric cameras from Ophir [79]. Pyrocam III has a resolution of 124 × 124 pixels with a pitch of 100 μm. The latest model Pyrocam IV has a higher resolution of 320 × 320 pixels with a pitch of 80 μm.

Microbolometers are bolometer detectors integrated on a chip. They measure the power of electromagnetic radiation indirectly via the temperature-dependent electrical resistance of the detector material, typically amorphous silicon, vanadium oxide, or silicon nitride. Microbolometers designed for infrared applications represent an established technology field, with typical resolutions of 640 × 480 pixels, even though arrays of up to 1280 × 960 pixels can be found [80]. For many practical applications, the scene imaged by the thermal detector is at room temperature, where the noise content of the image is dominated by the thermal radiation noise. The use of uncooled array detectors is generally sufficient, as thermal noise from such a camera is on the same order as that from the scene. Microbolometers have been intensively applied for long-wave infrared coherent imaging [81]. Interestingly, the microbolometers designed for the wavelength range 8–14 μm possess better sensitivities than THz microbolometers around 100 μm [82] and thus have become the cameras of choice for lensless imaging applications [35,36,83–87]. Notice that, however, care should be taken because their pixels are venerable to dazzling or permanent damage caused by a low-power (several μW) laser focused on several pixels. For a review on the use of uncooled bolometer-type infrared detectors for real-time THz imaging, see also [88,89]. Microbolometers specifically designed for THz radiation include cameras from the National Optics Institute (INO, Québec, Canada) [90], the NEC Corporation (Tokyo, Japan) [91], and the French Alternative Energies and Atomic Energy Commission (CEA Leti) [92,93].

Detection of sub-THz radiation at room temperature is often realized with Schottky-barrier diodes (SBDs) or field effect transistors (FETs) [94,95]. The detection mechanism of SBDs and FETs is based on the rectification process of electromagnetic signals. At low radiation powers, the output voltage is proportional to the input power. Both SBDs and FETs show response times below 10 ps at room temperature, and can be assembled into arrays [96,97].

D. Source–Detector Systems

Sub-THz radiation is the probe of choice for the investigation of dielectrics such as clothes, building materials, 3D printing filaments, and composites, as their absorption coefficient increases drastically when the frequency exceeds 1 THz [3,98,99]. The

long wavelength implies that a fairly large numerical aperture (NA) should be employed to achieve an appropriate lateral resolution. For instance, in [100], when working at 0.495 THz ($\lambda = 606$ μm), for a sample located 16.3 cm away from the detector, a detection area of 20×20 cm is needed to achieve a lateral resolution comparable to the wavelength. To the authors' knowledge, most published works on lensless imaging at sub-THz band have been done using a raster-scanned single detector, due to the lack of large enough 2D arrays with adequate sensitivity [9].

Materials such as polyethylene, polypropylene, polystyrene, poly tetrafluoroethylene (Teflon) [101,102], thin textiles [103], or dehydrated biological tissues [104] should be probed at frequencies above 1 THz, as they maintain high transparency, and images at better resolution can be obtained. The first reports on successful camera-based THz holography used the pyroelectric detector Pyrocam III [105,106]. In later works, models with higher resolutions were used [107]. Decent signal-to-noise ratios (SNRs) can be achieved with pyroelectric cameras at the strongest line (2.52 THz) of far-infrared gas lasers (FIRLs), after multi-frame averaging and dead pixel replacement procedures to improve the SNR [106,108,109]. However, the rather large sample pitch of 80–100 μm set a limit to the off-axis angle in off-axis digital holography. A comparison of four area detectors for their use in THz off-axis digital holography and real-time THz imaging was presented by Hack *et al.* [82]. According to them, the tested uncooled microbolometers are 40 times more sensitive than the pyroelectric camera Pyrocam III. As a consequence, the high detectivity of infrared microbolometers allows working with mW-level output sources such as QCLs or various FIRL lines [82,110–113]. Their pixel pitch of 17–25 μm is ideal for off-line holography, as it allows large off-axis angles. Moreover, their frame rate can go up to 50 Hz, enabling real-time imaging [114].

Representative imaging configurations, using cameras or scanning single-pixel detectors, are summarized in Table 1. The imaging techniques of these works will be detailed in the next section.

3. COHERENT LENSLESS IMAGING TECHNIQUES

A. General Remarks

Despite most coherent lensless imaging techniques using THz radiation bear no difference from the corresponding implementations at shorter wavelengths, e.g., with visible light, x rays, or electrons, the tremendous increase in wavelength has a relevant impact on the design and analysis of a THz imaging experiment.

From here on, we will describe the amplitude and phase modulation imposed by an unknown object, be it probed in transmission or in reflection, with a two-dimensional (2D) complex function on the plane of the object $o(\mathbf{x})$, with $\mathbf{x} \equiv (x, y)$. Radiation at the wavelength λ normally impinging on the object is diffracted at angles $\gamma_{x,y}$ with respect to the x, y axis given by $\cos(\gamma_{x,y}) = \lambda f_{x,y}$ [129], where $\mathbf{f} \equiv (f_x, f_y)$ is the spatial frequency coordinate corresponding to $\mathbf{x}$. While this makes the requirements on the dynamic range less stringent when using THz radiation, minimizing the object–detector distance becomes the most crucial issue in THz imaging. In practical cases, the camera housing sets a lower limit to the object–detector distance around $d \approx 5$ mm. A reasonable estimate of the incident beam size in all full-field, THz coherent lensless imaging techniques amounts to $w \approx 5$ mm, which translates to a Fresnel number $N_F \equiv w^2/(\lambda d) = 50$ at $\lambda = 0.1$ mm. Therefore, the far-field (or Fraunhofer) approximation, commonly employed in optical [130], x-ray [30], and electron [32] imaging, breaks down. In what follows, a generic complex wavefront $g(\mathbf{x})$ (representing, e.g., the object function at the object plane) will be propagated to a parallel plane at a distance $|L|$, thus yielding the propagated wavefront $G(\mathbf{x})$ (representing, e.g., the wavefront diffracted by the object function at the detector plane), through the following convolution, indicated with the symbol $*$:

$$G(\mathbf{x}) = g(\mathbf{x}) * h_L(\mathbf{x}). \tag{1}$$

Here, $h_L(\mathbf{x})$ is the Rayleigh–Sommerfeld convolution kernel [129], which has been obtained assuming only the scalar diffraction regime, and a propagation by $|L| \gg \lambda$ through a homogeneous and isotropic medium. It is given by

$$h_L(\mathbf{x}) \equiv \frac{|L|}{i\lambda} \frac{\exp[2\pi i \,\mathrm{sgn}(L)\sqrt{|\mathbf{x}|^2 + L^2}/\lambda]}{|\mathbf{x}|^2 + L^2}, \tag{2}$$

where $L > (<)0$ denotes forward (backward) propagation, and $\mathrm{sgn}(\cdot)$ is the sign function. The relatively high Fresnel numbers also make the angular spectrum propagation operator an alternative suitable choice in THz imaging [106].

B. Resolution in Coherent Lensless Imaging

Like all conventional imaging techniques, all the coherent lensless imaging techniques presented in this contribution are subject to the diffraction limit, i.e., the lateral resolution ρ_{lat} depends on the wavelength and the NA according to $\rho_{\mathrm{lat}} = \lambda/(2\ \mathrm{NA})$. In the absence of imaging components such as lenses, NA at a generic position $\mathbf{x}$ on the reconstructed wavefront is set only by the angle η subtended by the detector size from $\mathbf{x}$, so

$$\rho_{\mathrm{lat}} = \frac{\lambda}{2\sin(\eta)}, \tag{3}$$

where a refractive index of 1 has also been assumed. Although the best achievable lateral resolution is limited by Abbe's limit $\lambda/2$, much finer features can be resolved along the longitudinal direction. For example, in the reconstruction of an object with refractive index n, measured in transmission at normal incidence, a phase difference of $\Delta\phi$ between two points relates to a thickness difference $\Delta t = \Delta\phi\lambda/[2\pi(n-1)]$. In these conditions, it is the phase resolution ρ_ϕ that determines the depth resolution ρ_{depth}, as follows:

$$\rho_{\mathrm{depth}} = \frac{\rho_\phi \lambda}{2\pi(n-1)}, \tag{4}$$

which can lead to values of ρ_{depth} as low as about $\lambda/91$ [112].

In the following sections, the coherent lensless imaging techniques demonstrated using THz radiation will be discussed. For

Table 1. Combinations of Sources and Detectors Used for THz Lensless Imaging

Source	Source Frequency	Detector	Scan Area/Array Size	Scan Step/Pixel Pitch	References
Gunn diode	0.1 THz	SBD	150 × 150 mm	Not available	[115]
Gunn diode	0.1 THz	SBD	297 × 297 mm	2.32 mm	[116]
Gunn diode	0.17 THz	Pyrocam III	124 × 124	100 μm	[117]
Gunn diode	0.31 THz	SBD	400 × 400 mm	0.5 mm	[118]
Multiplier chain	0.495 THz	Heterodyne receiver	200 × 200 mm	0.2 mm	[100]
Multiplier chain	0.712 THz	SBD	80 × 80 mm	0.5 mm	[119]
BWO	0.58 THz	SBD	50 × 50 mm	0.5 mm	[120]
QCL	3.0 THz	Devitech IR-032	640 × 480	25 μm	[83]
QCL	2.8 THz	Miricle307	640 × 480	25 μm	[85]
QCL	3.0, 4.4 THz	NEC IRV-T0831	320 × 240	23.5 μm	[110–113,121]
FIRL	2.52 THz	Pyrocam III	124 × 124	100 μm	[105,106,108,122–125]
FIRL	2.52 THz	Pyrocam IV	320 × 320	80 μm	[107,126,127]
FIRL	2.52 THz	Devitech IR-032	640 × 480	25 μm	[84]
FIRL	2.52, 3.1 THz	Xenics Gobi-640	640 × 480	17 μm	[35,36,86,114,128]
FIRL	5.24 THz	IRay Technology	640 × 512	17 μm	[87]

each technique, a theoretical overview as well as a summary of the published results will be provided.

C. Digital Holography

Holography reconstructs the object function $o(\mathbf{x})$ by recording the intensity of the interference pattern between the wavefront diffracted by $o(\mathbf{x})$ at the detector, referred to as "object beam" $O(\mathbf{x})$, and a coherent wave that does not interact with the object and is referred to as "reference beam" $R(\mathbf{x})$, yielding the following distribution known as a "hologram":

$$I(\mathbf{x}) \equiv |R(\mathbf{x}) + O(\mathbf{x})|^2. \tag{5}$$

Originally developed by Gabor in 1948 to replace conventional imaging techniques in electron microscopy [131], it is nowadays mostly performed with electromagnetic radiation. Owing to the recent increased computational capabilities of digital devices, the reconstruction has evolved from an analogue to a fully numerical procedure. Digital holography has therefore turned into the coherent lensless imaging technique of choice for many applications in biology, materials science, and mechanical engineering (see, e.g., [33,132–135]).

1. Off-axis Digital Holography

In one variant of digital holography, named "off-axis" [Fig. 1(a)], the reference beam and the object beam travel along different directions. We denote their complex wavefront at the detector plane by $U(\mathbf{x}) \equiv A_U(\mathbf{x}) \exp\{i[\mathbf{k}_U \cdot \mathbf{x} + \phi_U(\mathbf{x})]\}$, where $A_U(\mathbf{x})$ is the amplitude, $\phi_U(\mathbf{x})$ is the phase when observed across a plane perpendicular to the average wavevector $\mathbf{k}_U$, and $U \in \{R, O\}$ labels the reference beam (R) and the object beam (O).

The hologram of Eq. (5) thus becomes

$$I(\mathbf{x}) \equiv A_R^2(\mathbf{x}) + A_O^2(\mathbf{x}) + 2A_R(\mathbf{x})A_O(\mathbf{x}) \times \cos[(\mathbf{k}_R - \mathbf{k}_O) \cdot \mathbf{x} + \phi_R(\mathbf{x}) - \phi_O(\mathbf{x})]. \tag{6}$$

The angle θ between $\mathbf{k}_R$ and $\mathbf{k}_O$ [displayed in the inset of Fig. 1(a)] modulates $I(\mathbf{x})$ [Fig. 1(b)] at the spatial carrier frequency $\mathbf{f}_c$, with modulus $\sin(\theta)/\lambda$ and same direction as $\Delta\mathbf{k} \equiv \mathbf{k}_R - \mathbf{k}_O$ on the Fourier plane. The Fourier transform of $I(\mathbf{x})$, $\mathcal{I}(\mathbf{f})$ [whose modulus is shown in Fig. 1(c)], features a DC component at the spatial frequency $\mathbf{f} = (0, 0)$, the +1st diffraction order $\mathcal{C}(\mathbf{f} - \mathbf{f}_c)$ at $\mathbf{f} = \mathbf{f}_c$, and the −1st diffraction order $\mathcal{C}^*(\mathbf{f} + \mathbf{f}_c)$ at $\mathbf{f} = -\mathbf{f}_c$, where $\mathcal{C}(\mathbf{f})$ is the Fourier transform of $c(\mathbf{x}) \equiv A_R(\mathbf{x})A_O(\mathbf{x}) \exp\{i[\phi_R(\mathbf{x}) - \phi_O(\mathbf{x})]\}$. Following the widespread Fourier transform demodulation technique developed by Takeda *et al.* [137], provided that (i) $\mathbf{f}_c$ is large enough to prevent $\mathcal{C}(\mathbf{f} - \mathbf{f}_c)$, $\mathcal{C}^*(\mathbf{f} + \mathbf{f}_c)$, and $\mathcal{A}(\mathbf{f})$ from overlapping; and (ii) the amplitude $A_R(\mathbf{x})$ and phase $\phi_R(\mathbf{x})$ of the reference beam are known or can be measured at a preliminary stage, then $A_O(\mathbf{x})$ and $\phi_O(\mathbf{x})$ are retrieved upon taking the modulus and the argument of $c(\mathbf{x})$, respectively, after selecting $\mathcal{C}(\mathbf{f} - \mathbf{f}_c)$ by filtering $\mathcal{I}(\mathbf{f})$.

Since the detector plane is typically oriented perpendicularly to $\mathbf{k}_O$, the wavefront diffracted by the object can be simplified to $O(\mathbf{x}) = A_O(\mathbf{x}) \exp[i\phi_O(\mathbf{x})]$. The reconstruction of $o(\mathbf{x})$ is obtained by back-propagating $O(\mathbf{x})$ by the object–detector distance d through the propagation kernel of Eq. (2):

$$o(\mathbf{x}) = O(\mathbf{x}) * h_{-d}(\mathbf{x}). \tag{7}$$

If, like in the setup in Fig. 1(a), the object is tilted with respect to the detector plane, the reconstructed wavefront appears skewed [Figs. 1(d) and 1(e)]. A rotational transformation [138,139] may be finally applied to bring the reconstructions to the reference frame of the object.

Off-axis holography was the first variant of digital holography ever implemented with THz radiation, performed in transmission mode. Mahon *et al.* first demonstrated an off-axis THz digital holography configuration using a 100 GHz Gunn diode oscillator and a SBD installed on a planar scanner to record the hologram pixel by pixel [115,140]. A Teflon sample inside an envelope was reconstructed with a lateral resolution of 9 mm (3λ). In 2011, Heimbeck *et al.* proposed a THz off-axis digital holography geometry based on a Mach–Zehnder

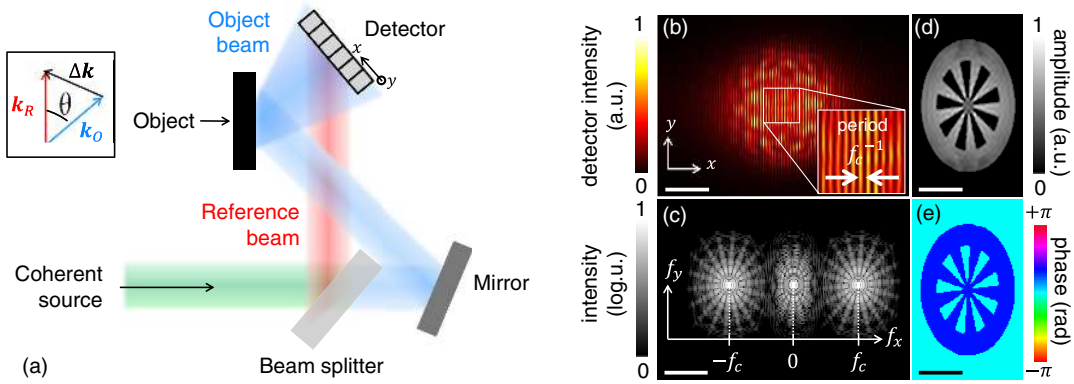

Fig. 1. Schematic of off-axis digital holography (simulations). (a) Experimental setup; (b) hologram and (c) modulus of its Fourier transform; (d) amplitude and (e) phase of the reconstructed object function. The inset of (a) shows the average wavevectors of the object beam and reference beam, as well as their difference. Wavelength: 96.5 μm. Scale bars in (b), (d), and (e): 2 mm; scale bar in (c): 5mm^{-1}. Adapted with permission from [136].

interferometer [119]. The off-axis holograms were recorded with a Schottky diode square law detector, combined with a lock-in amplifier and mounted on a 2D linear stage. Tuning the emission frequency in the range of 0.66–0.76 THz through a frequency-multiplied microwave synthesizer allowed the use of a dual-wavelength approach to eliminate the 2π phase ambiguity problem for optical path differences as large as the synthetic wavelength. Note that this well-known multi-wavelength technique has also been developed in other THz interferometry setups for, e.g., thickness measurement applications [141,142]. The first actual "full-field" implementation was provided by Ding *et al.* using a 2.52 THz optically pumped THz laser and a pyroelectric detector with 124 × 124 pixels and obtaining a lateral resolution of about 0.4 mm (3.4λ) [105]. By shortening the recording distance, Li *et al.* [122] pushed the resolution down to 0.245 mm (2.1λ). In 2014, Hack and Zolliker used a 3 THz non-monochromatic QCL and an uncooled microbolometer array detector to build an off-axis setup based on a Lloyd's interferometer [83]. A metallic Siemens star and a patterned polypropylene slab were reconstructed with a lateral resolution of 0.280 mm (≈ 2.8λ) and a phase resolution of 0.5 rad, corresponding to a depth resolution of 16 μm according to Eq. (4). Shortly afterwards, Yamagiwa *et al.* reported reconstructions of optically opaque plastic and silicon plates with a depth resolution of 1.1 μm (λ/91) [112].

An off-axis digital holographic setup conveniently lends itself to reconstructions in reflection mode, too. The first implementation with THz radiation was reported by Cherkassky *et al.* [73]. Quasi-CW THz radiation was generated by a Novosibirsk high-power FEL in the wavelength range of 120–180 μm. Holograms were indirectly recorded via a combination of digital video camera and InAs near-infrared thermograph. In 2008, Tamminen *et al.* proposed a THz off-axis digital holographic setup for reflective objects placed 1.5 m away from the detector, reaching resolutions between 4 mm and 8 mm (4 − 8λ) [118].

Later on, Zolliker and Hack proposed a THz off-axis digital holography setup in reflection, where resolution enhancement was achieved via a synthetic aperture acquisition [84] borrowed from the radar imaging community [143]. The system included a movable mirror to produce phase-shifted holograms, and the detector was moved across its detection plane so as to synthesize a hologram with an area 3.5 times larger than the detector area, after stitching 19 partially overlapping holograms. The obtained lateral and depth resolutions were 200 μm (≈ 1.7λ) and 6 μm (≈ λ/20), respectively. Locatelli *et al.* successfully reconstructed in real time a moving metallic plate [Fig. 2(a)], both when it was directly seen by the detector [Fig. 2(b)] and when it was hidden behind an optically opaque polypropylene mask [Figs. 2(c) and 2(d)] [85]. With a similar setup, Valzania *et al.* proposed a systematic procedure to suppress the spurious reflections from a cover plate hiding an object from the camera field of view, thereby improving the reconstruction of the hidden object [35]. Humphreys *et al.* reported the first video rate (50 Hz) THz off-axis digital holography reconstructions, achieving a resolution of 280 μm (2.4λ) [114]. Recently, Wang *et al.* used a widespread sub-pixel image registration algorithm [144] and image stitching to expand the reconstructed field of view [126]. After a comparison with reference measurements with a surface profiler, they estimated a relative error of 3% and 6% in the reconstruction of a gold plated bookmark when it was not covered and covered by a Teflon plate, respectively.

2. *In-line Digital Holography*

In in-line digital holography, which is the variant originally conceived by Gabor, the reference beam and the object beam travel along the same direction before impinging on the detector. To allow such a scheme, the object must be smaller than the incident beam, or it should impose a weak modulation, such that a portion of the incident beam is not affected by the object and can act as a reference beam, interfering with the part of the beam being diffracted and playing the role of the object beam [Fig. 3(a)]. Figure 3 illustrates the principle using the simulated pure phase object displayed in Fig. 3(b) and the hologram in Fig. 3(c).

Using the superscript * to denote complex conjugation, we rewrite Eq. (5) as

$$I(\mathbf{x}) = |R(\mathbf{x})|^2 + |O(\mathbf{x})|^2 + O^*(\mathbf{x})\,R(\mathbf{x}) + R^*(\mathbf{x})\,O(\mathbf{x}). \quad \textbf{(8)}$$

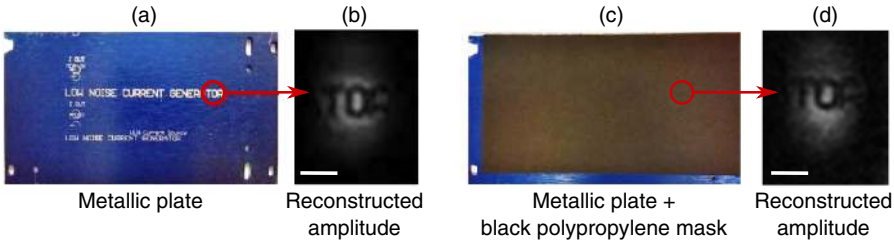

Fig. 2. THz off-axis digital holographic reconstructions in reflection mode of an object moving at 5 mm/s. (a) Photograph of the object, a metallic plate with inscriptions; (b) reconstructed amplitude of the object at one position during its movement; (c) photograph of the plate covered by an optically opaque mask; (d) reconstructed amplitude of the hidden object at the same position as in (b). Scale bars: 4 mm. Adapted from [85] under the terms of the Creative Commons Attribution 4.0 License.

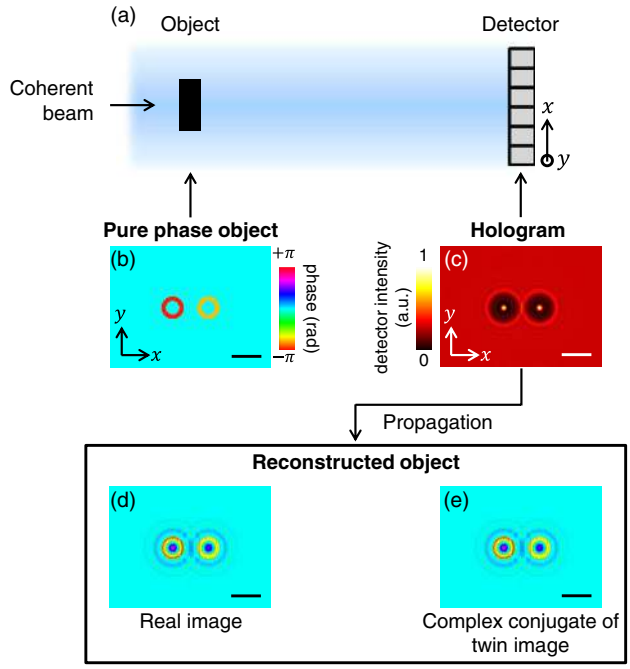

Fig. 3. Schematic of in-line digital holography (simulations). (a) Experimental setup; (b) simulated phase object and (c) corresponding hologram; (d) reconstruction where the (d) real [(e) twin] image is brought to focus. In (e), the complex conjugate of the reconstruction is shown, to favor its comparison with (d). Wavelength: 96.5 μm. Scale bars: 2 mm.

Illuminating the hologram with the reference beam another time yields the following distribution:

$$\begin{aligned} R(\mathbf{x})\,I(\mathbf{x}) &= R(\mathbf{x})|R(\mathbf{x})|^2 + R(\mathbf{x})|O(\mathbf{x})|^2 \\ &\quad + O^*(\mathbf{x})\,R^2(\mathbf{x}) + |R(\mathbf{x})|^2\,O(\mathbf{x}) \\ &\approx O^*(\mathbf{x}) + O(\mathbf{x}), \end{aligned} \tag{9}$$

where the approximation holds under the assumptions that $|O(\mathbf{x})| \ll |R(\mathbf{x})|$, the reference beam is a plane wave normally impinging on the detector, i.e., $R(\mathbf{x}) =$ constant, and the constant background and factors have been omitted. A back-propagation of such a distribution by the object–detector distance d, using the fact that, apart from a constant phase factor, $h_L^*(\mathbf{x}) = h_{-L}(\mathbf{x})$ [see Eq. (2)], leads to the distribution

$$[R(\mathbf{x})\,I(\mathbf{x})] * h_{-d}(\mathbf{x}) \approx o^*(\mathbf{x}) * h_{-2d}(\mathbf{x}) + o(\mathbf{x}), \tag{10}$$

whose phase is shown in Fig. 3(d), featuring the reconstructed object $o(\mathbf{x})$ superimposed with an out-of-focus image of $o^*(\mathbf{x})$, referred to as "twin image." Conversely, forward propagating the last side of Eq. (9) by d brings the twin image $o^*(\mathbf{x})$ in focus and the real image $o(\mathbf{x})$ out of focus [see Fig. 3(e), where the complex conjugate of the twin image is shown, which is equivalent to the real image]. The overlap of these two distributions worsens the reconstruction of $o(\mathbf{x})$, and solutions have been suggested to cope with the twin image problem, employing mostly iterative phase retrieval procedures that will be detailed in the next section (see, e.g., [145–147]).

Compared with the off-axis variant, in-line digital holography represents a more compact solution featuring a shorter reconstruction distance and consequently a higher resolution, although it is suited only for isolated or almost transparent objects. Xue *et al.* performed CW THz in-line digital holography [148], increasing the lateral resolution by a factor of two compared to [105] (1.7λ as opposed to 3.4λ), and demonstrated its effectiveness in imaging hidden objects [122]. Hu *et al.* thoroughly investigated different amplitude, phase, and support constraints on the object plane as well as zero padding of holograms, boundary replication expansion, and apodization to improve the iterative phase retrieval in THz in-line digital holography [123,124]. Upon recording two sets of in-line holograms at different distances [149], Li *et al.* departed from the conventional in-line digital holographic reconstruction procedure, gradually blurring the boundary between in-line digital holography and phase retrieval. Further, they recorded holograms translated by sub-pixel distances to yield a finer hologram sampling, and they overall achieved a lateral resolution of 1.3λ. Rong *et al.* combined the phase retrieval algorithm from [145] with a hologram extrapolation method [150] to suppress the twin image and enhance the lateral resolution of a dragonfly hindwing, revealing features of 35 μm (≈λ/3) [106]. While hologram extrapolation has the advantage of being a post-processing tool, which does not impact the acquisition time of the experiment, it can provide only a guessed solution in the regions that were not measured. As an alternative, a synthetic aperture scheme uses real holograms to increase the resolution, and is an effective solution for THz in-line digital holography, as well. Examples were reported in [110,111], reconstructing features as low as λ. In Ref. [108], THz in-line digital holography

was implemented toward a medical application. The reconstruction of a hepatocellular carcinoma tissue slice [Fig. 4(a)] proved that early signs of liver cancer and diseases can be traced to the phase of a reconstructed THz hologram. Although the reconstructions from one hologram [Figs. 4(b) and 4(c)] did not provide enough insight, increasing the resolution through synthetic aperture acquisition [Figs. 4(d) and 4(e)] and in combination with numerical hologram extrapolation [Figs. 4(f) and 4(g)] revealed a sign of tissue fibrosis, thus making THz coherent lensless imaging a promising tool for cancer diagnosis, with the potential to complement conventional histopathological analyses.

Recently, Li *et al.* reported a resolution of 0.7λ adding a L_1-sparsity constraint to the support constraint at the object plane [87]. Further strategies for the correction of experimental inaccuracies were reported. Chen *et al.* developed a denoising method for THz in-line digital holographic reconstructions, based on a Markov chain Monte Carlo sampling [151]. Different auto-focusing algorithms and corrections were investigated by Huang *et al.* [125,127] and applied to reconstruct a pair of objects at different distances from the detector [121].

D. Phase Retrieval

Phase retrieval imaging techniques aim at reconstructing the object function $o(\mathbf{x})$ from the intensity of its diffraction pattern $I_j(\mathbf{x})$ measured at one or multiple distances d_j, $j = 1, 2, \ldots, J$, as shown at the top of Fig. 5, i.e.,

$$I_j(\mathbf{x}) = |o(\mathbf{x}) * h_{d_j}(\mathbf{x})|^2. \tag{11}$$

Although the acquisition setup recalls that of in-line digital holography, if we assume $J = 1$ (Fig. 3), the reconstruction procedure is essentially different from the one outlined in Section 3.3.2, the main difference being that phase retrieval techniques need not model a reference beam. This makes the experimental constraints easier to meet, as the object is allowed to be strongly diffracting and even have a size comparable to that of the incident beam.

We assume that each $I_j(\mathbf{x})$ is sampled with $N \times N = N^2$ pixels, and that $o(\mathbf{x})$ is unknown on a number of pixels $M^2 \leq N^2$. Because both the amplitude and the phase of $o(\mathbf{x})$ have to be determined, the total number of unknowns amounts to $2M^2$. Using the definition of oversampling ratio given by Miao *et al.* [152],

$$\sigma \equiv \frac{\text{total number of pixels}}{\text{number of pixels of unknown value}} = \frac{N^2}{M^2}, \tag{12}$$

we can therefore conclude that an oversampling ratio $\sigma = 2$ is needed in order to invert the system of Eq. (11). In real experiments, however, the presence of noise requires redundant information, so typically $\sigma \gg 2$ is preferred. Each phase retrieval technique aims at increasing the oversampling ratio in at least one of the following ways:

- by increasing the total number of pixels N^2, collecting several ($J > 1$) diffraction patterns described by Eq. (11) at different distances from the object [153,154];
- by decreasing the number of pixels of unknown value M^2, using *a priori* knowledge on the object function at some locations [31]. Because usually the approximate spatial extent of the object or of the incident beam is known, such *a priori* information is referred to as "support constraint."

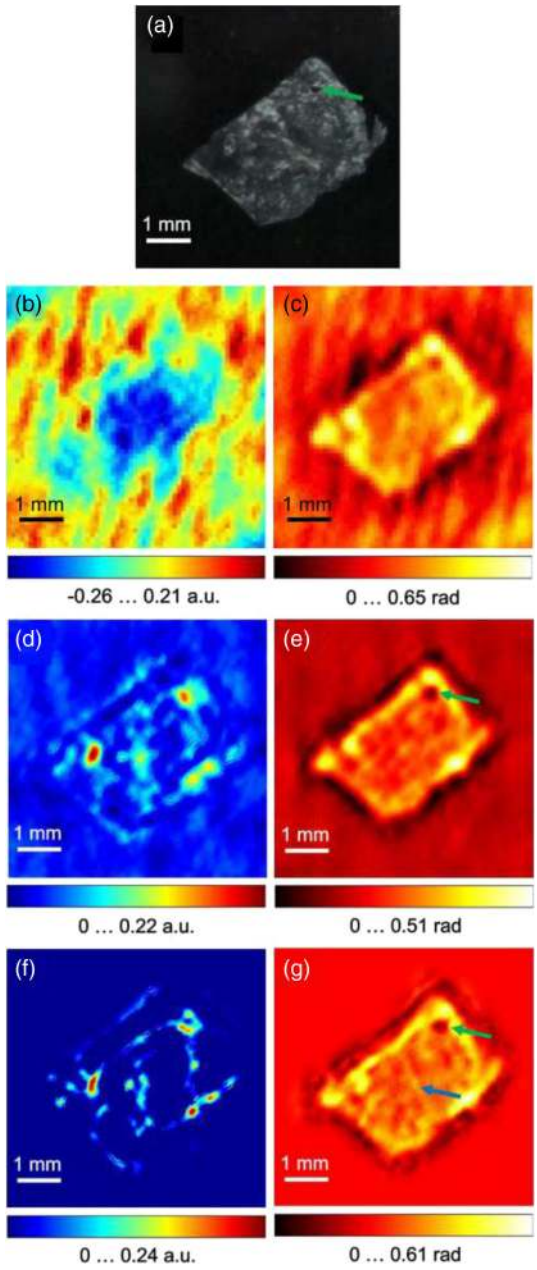

Fig. 4. THz in-line digital holographic reconstructions. (a) Photograph of the object, a human hepatocellular carcinoma tissue; (b) reconstructed absorption and (c) phase shift from a single 12.4 × 12.4 mm² hologram; (d) reconstructed absorption and (e) phase shift from a larger hologram obtained through aperture synthesis; (f) reconstructed absorption and (g) phase shift after numerically extrapolating the holograms used for reconstructions (d) and (e). The green arrow indicates a cut across a vessel or a region damaged after freezing the object. The blue arrow indicates a vertical line that is a sign of tissue fibrosis, which can be resolved only in (g). Adapted from [108] under the terms of the Creative Commons Attribution 4.0 License.

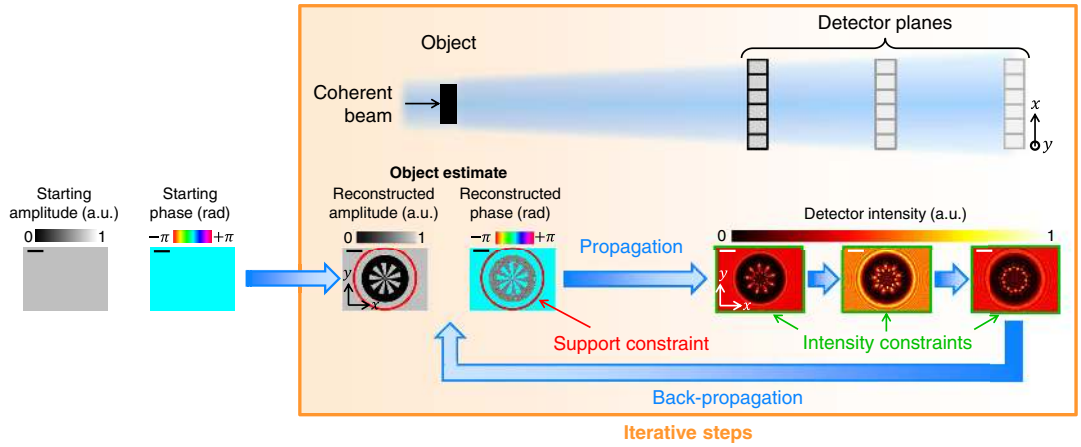

Fig. 5. Steps of a typical phase retrieval technique, using three diffraction patterns recorded at different distances from the object (simulations). Wavelength: 96.5 μm. Scale bars: 2 mm.

Therefore, a typical iterative phase retrieval procedure proceeds according to these steps, graphically summarized in Fig. 5:

1. Construct a first estimate of $o(\mathbf{x})$, usually by assigning a constant or random distribution to its amplitude and phase (left-hand side of Fig. 5). If available, a support constraint, represented with a red circle in Fig. 5, is applied.
2. Propagate the current estimate of $o(\mathbf{x})$ to the first detector plane through the propagation kernel of Eq. (2). Apply the so-called "intensity constraint," replacing the calculated amplitude of the propagated wavefront with the square root of the measured intensity at that detector plane, while keeping the phase unchanged.
3. Propagate the corrected wavefront to the next detector plane, if any, and apply the intensity constraint again using the diffraction pattern recorded at the corresponding plane. Repeat this operation for every remaining detector plane (Fig. 5 shows the process for $J = 3$).
4. Back-propagate the last corrected wavefront to the object plane, where the support constraint is applied again.
5. Iterate steps 2–4, enclosed in the orange box in Fig. 5, until a suitably defined error function becomes lower than a predefined threshold.

1. Two-intensity Techniques

Using the diffraction patterns recorded at two detector planes, which increases the oversampling ratio by a factor of two, may not be enough for a phase retrieval algorithm to converge to the sought solution [155]. In this case, to further increase the oversampling ratio and lower the chance that the algorithm stagnates in a local minimum, M^2 is decreased to values much lower than N^2 through a support constraint.

A phase retrieval technique of this kind was performed by Hislop *et al.* using THz radiation [120]. The THz source was a BWO operating at 0.58 THz and the detector was a Schottky diode, sensitive only to the power of the incident THz radiation and scanned across two 50×50 mm^2 planes, with a relative distance of about λ, i.e., 0.5 mm [Fig. 6(a)]. Their reconstruction technique, referred to as the "successive projections method" [155], reproduced a standard iterative phase retrieval procedure like the one outlined in the previous section, where the knowledge of the incident beam was used as a support constraint. Two additional constraints were applied to favor convergence. The first one consisted of updating the low spatial frequencies of the object function during the first iterations, and subsequently allowing the reconstruction to be refined at higher and higher spatial frequencies. Notice that such a constraint is essentially another way to reduce the number of pixels with unknown value M [see Eq. (12)] in the first iterations, thereby increasing the oversampling ratio. The second constraint represented a modified version of the intensity constraint, where the calculated diffracted amplitude at the jth detector plane $A_j(\mathbf{x})$ was averaged with the square root of the corresponding measured intensity $\sqrt{I_j(\mathbf{x})}$, yielding the corrected estimate of the wavefront at the jth detector plane $A'_j($, as follows:

$$A'_j(\mathbf{x}) \equiv (1-\beta)A_j(\mathbf{x}) + \beta\sqrt{I_j(\mathbf{x})}. \tag{13}$$

The real parameter β, known as the "over projecting factor," decreases its value from ≈ 3 to 1 with increasing iterations and helps the algorithm reach the global minimum of the error function, avoiding stagnation in local minima. When approaching the last iterations, i.e., $\beta = 1$, Eq. (13) reduces to the standard intensity constraint $A'_j(\mathbf{x}) \equiv \sqrt{I_j(\mathbf{x})}$. The performance of the algorithm was demonstrated by successfully reconstructing a metallic thumbtack in transmission mode [Figs. 6(b) and 6(c)].

2. Multiple-intensity Techniques

As opposed to two-intensity phase retrieval techniques, multiple-intensity methods employ diffraction patterns collected at $J > 2$ planes in order to increase the oversampling ratio to values greater than 2, obviating the need for a support constraint.

The single-beam multiple-intensity reconstruction (SBMIR) technique [154,156] follows the typical five steps of phase retrieval techniques to reconstruct $o(\mathbf{x})$ with no *a priori* knowledge on it.

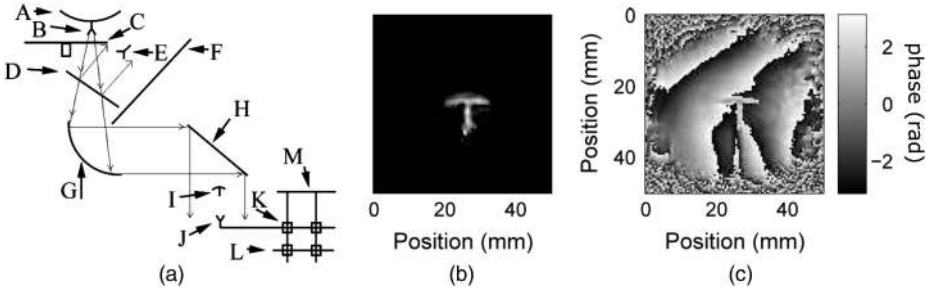

Fig. 6. Two-intensity phase retrieval. (a) Schematic experimental setup, featuring: a BWO (A) with its waveguide opening (B), a chopper (C), a beam splitter made of non-conducting silicon (D), a detector to monitor the stability of the source (E), a beam stopper to prevent the THz radiation emitted by the source from directly reaching the receiver (F), mirrors (G), (H), a metallic thumbtack used as the object (I), and the receiver (J) moved longitudinally through two sliding blocks (K), (L) and transversely through a 2D stage (M). (b) Amplitude of the reconstructed object and (c) phase of the object and of the incident beam. Adapted with permission from [120] 2019 IEEE.

The optimum acquisition parameters of a SBMIR experiment have been discussed in [156–158] and in the supplementary document of [36]. The minimum object–detector distance theoretically allowed must guarantee that the highest spatial frequencies of the wavefront diffracted by the object at the detector plane are sampled by the detector pixels without alising. This implies that $\sin(\zeta/2) < \lambda/(4p)$, where ζ is the angle under which a point on the detector centered with the object sees the object, and p is the pixel pitch. Since at THz wavelengths, $\lambda \approx 100$ μm, and for currently available digital cameras, $p \approx 20$ μm, $\lambda/(4p) > 1$, i.e., there are no restrictions (or no stringent restrictions in case longer wavelengths are used) on the minimum object–detector distance, with a positive impact on the NA and consequently on the lateral resolution.

The distance between consecutive detector planes should ensure that each new diffraction pattern provides both redundant and additional information to allow the phase to be iteratively retrieved. A reasonable estimate of the propagation length after which a diffraction pattern at the object–detector distance d has changed is the depth of focus DOF, scaling with the size w of the illuminated region according to [129]

$$\mathrm{DOF} \approx \lambda \left(\frac{d}{w}\right)^2. \tag{14}$$

For example, imaging a field of view of $w = 5$ mm at the wavelength $\lambda = 0.1$ mm and at a distance $d = 10$ mm yields $\mathrm{DOF} = 0.4$ mm.

Once the minimum object–detector distance as well as the distance between consecutive detector planes is fixed, the number of diffraction patterns should be chosen by carefully considering that the larger the object–detector distance, the lower the resolution of the diffraction pattern due to a lower NA, and the higher the chance that it will be corrupted by noise caused by, e.g., experimental misalignments and laser power loss through absorption during the propagation, resulting in a detrimental effect on the reconstruction. Although the optimum acquisition parameters vary with the object to be reconstructed, we have found that in all the implementations using THz radiation, up to five diffraction patterns have been used at a DOF ranging from 0.5 to 1 mm and at a minimum object–detector distance larger than ≈ 5 mm [36,120].

An example of THz SBMIR reconstructions will be discussed in the next section, as part of a phase retrieval technique for imaging behind a moving and scattering barrier.

3. *Phase Retrieval Technique for Imaging behind a Moving and Scattering Barrier*

Recently, an imaging technique reconstructing two objects stacked one behind the other in transmission mode has been developed and experimentally demonstrated with THz radiation [36].

A schematic setup is shown in Fig. 7(a). We denote the transmission functions of the two objects with $b(\mathbf{x})$ and $o(\mathbf{x})$, where "b" stands for the barrier and "o" for the object hidden behind it at a distance u. When a plane wave with unit amplitude impinges on the hidden object, the wavefront $\Psi(\mathbf{x})$ at a plane perpendicular to the optical axis and at the distance d from the barrier can be written as

$$\Psi(\mathbf{x}) = \{[o(\mathbf{x}) * h_u(\mathbf{x})]b(\mathbf{x})\} * h_d(\mathbf{x}), \tag{15}$$

where we have assumed the two objects are thin enough, such that their interaction with the corresponding incident wavefront can be described through the multiplicative approximation [32]. Nevertheless, we point out that no assumptions on $b(\mathbf{x})$ and $o(\mathbf{x})$ have been made, therefore allowing either object to strongly diffract its corresponding incident beam.

Provided that one object is transversely shifted with respect to the other one, and the shifts are known, both transmission functions $o(\mathbf{x})$ and $b(\mathbf{x})$ can be retrieved, with no *a priori* information on them. Denoting the translations of the barrier with $\mathbf{x}_k, k = 1, 2, \ldots, K$, Eq. (15) becomes

$$\Psi_k(\mathbf{x}) = \{[o(\mathbf{x}) * h_u(\mathbf{x})]b(\mathbf{x} - \mathbf{x}_k)\} * h_d(\mathbf{x}). \tag{16}$$

Now the reconstruction procedure relies on two steps:

1. Retrieve the wavefronts $\psi_k(\mathbf{x})$, referred to as "exit waves," at the exit of the barrier plane, namely, the quantities

$$\psi_k(\mathbf{x}) \equiv [o(\mathbf{x}) * h_u(\mathbf{x})]b(\mathbf{x} - \mathbf{x}_k). \tag{17}$$

This is achieved through the SBMIR technique from Section 3.D.2, using the intensities of a set of J diffraction patterns $\Psi_{kj}(\mathbf{x})$ recorded at the distances d_j,

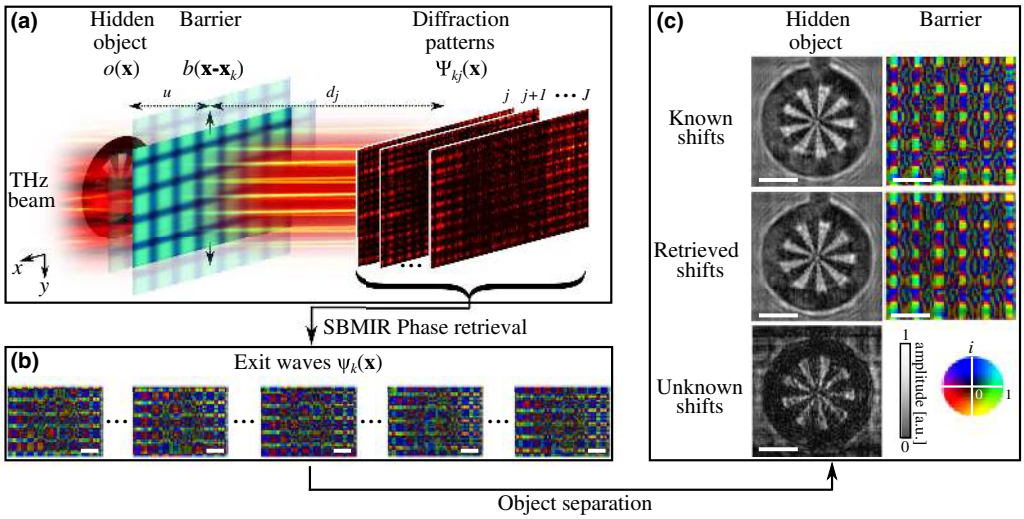

Fig. 7. Phase retrieval imaging behind a moving and scattering barrier. (a) Schematic experimental setup; (b) reconstruction of the wavefronts at the exit of the barrier plane through the SBMIR method; (c) reconstruction of the hidden object and the barrier (top row) assuming that the transversal shifts of the barrier are known *a priori*, (middle row) retrieving the shifts via cross-correlation, and (bottom row) assuming unknown shifts, which allows the reconstruction of the hidden object only. Scale bars: 2 mm. Adapted with permission from [159] The Optical Society.

$j = 1, 2, \ldots, J$ from the barrier, for each position of the barrier with respect to the hidden object [Fig. 7(b)], as follows:

$$|\Psi_{kj}(\mathbf{x})|^2 \equiv |\psi_k(\mathbf{x}) * h_{d_j}(\mathbf{x})|^2. \tag{18}$$

2. Recover the transmission functions $o(\mathbf{x})$ and $b(\mathbf{x})$, using the exit waves available from the previous step, and the transversal shifts $\mathbf{x}_k$.

Towards this goal, we notice that, despite the barrier being seen directly by the detector, its reconstruction is prevented because it is illuminated by a set of strongly non-uniform probes, represented by the wavefronts transmitted through the hidden object and shifted by the amounts $\mathbf{x}_k$. In order to enable a reliable reconstruction of $b(\mathbf{x})$, the authors proposed to wash out the high-frequency components of $o(\mathbf{x}) * h_u(\mathbf{x})$, so as to mimic a slowly varying probe incident onto the barrier. They achieved this by (i) compensating for the shift of the exit waves and (ii) averaging them. If we let $\mathcal{S}_{k=1}^{K}[f_k(\mathbf{x})]$ denote an operator performing these two operations on each amplitude or phase distribution $f_k(\mathbf{x})$ (see also the supplementary document of [36]), the estimated amplitude $|b(\mathbf{x})|$ and phase $\phi_b(\mathbf{x})$ of $b(\mathbf{x})$ read

$$|b(\mathbf{x})| \approx \mathcal{S}_{k=1}^{K}[|\psi_k(\mathbf{x})|], \tag{19a}$$

$$\phi_b(\mathbf{x}) \approx \mathcal{S}_{k=1}^{K}[\phi_{\psi_k}(\mathbf{x})]. \tag{19b}$$

Finally, the hidden object is obtained by dividing each exit wave by the barrier transmission function, and back-propagating the wavefront to the object plane:

$$o(\mathbf{x}) = \left\langle \frac{\psi_k(\mathbf{x})}{b(\mathbf{x}-\mathbf{x}_k)} \right\rangle_k * h_{-u}(\mathbf{x}), \tag{20}$$

where $\langle\cdot\rangle_k$ performs the average over all the configurations indexed by k.

The method was experimentally verified using THz radiation to reconstruct a glass fabric sample and a pure amplitude or a pure phase object hidden behind it. Upon translating the fabric across a 2D square grid of $20 \times 20 = 400$ points with a spacing of $\approx 0.8\lambda$, the authors could reconstruct the hidden objects with a depth resolution of $\approx \lambda/10$ and a lateral resolution of $\approx 1.5\lambda$ [see the top row of Fig. 7(c), showing the reconstructions for an amplitude object]. Furthermore, they demonstrated comparable results after retrieving the shifts $\mathbf{x}_k$ through cross-correlation on the measured diffraction patterns [middle row of Fig. 7(c)]. Most interestingly, they showed that reconstructing the hidden object is possible even when the shifts are unknown, or cannot be retrieved through cross-correlation [bottom row of Fig. 7(c)], thus suggesting promising applications for imaging behind dynamic scattering media.

4. Ptychography

Another coherent lensless imaging technique successfully implemented with THz radiation is ptychography [32]. Hoppe originally conceived the ptychographic method in 1969 as a new microscopic principle for imaging crystalline samples [160] and, like holography, in order to improve electron imaging, which suffered from poor imaging optics. In its simplest and most common implementation, ptychography iteratively reconstructs an object using a set of diffraction patterns, obtained upon scanning the object with a coherent beam with partially overlapping neighboring positions. The combination of the original ptychographic idea with iterative phase retrieval algorithms, suggested by Rodenburg and Faulkner [32,161], boosted the interest of the imaging community in ptychography. Several algorithms have been put forward, e.g., reconstructing the incident beam alongside the object [162–164], dealing with partially coherent radiation [165], or recovering the scan shifts between the beam and the object [166]. Ptychography has been heavily used with x rays [167], as

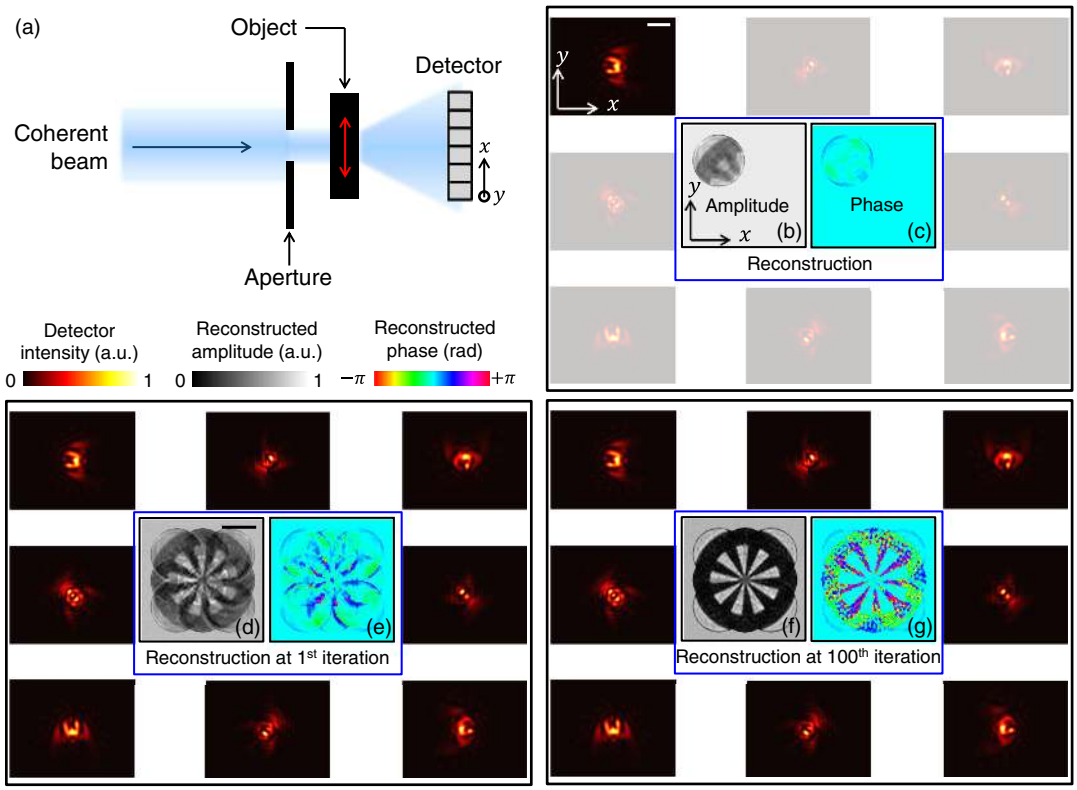

Fig. 8. Schematic of ptychography (simulations). (a) Experimental setup. (b) Amplitude and (c) phase of the object transmission function reconstructed from only the top-left diffraction pattern. (d) , (f) Amplitude and (e) , (g) phase of the object transmission function after 1 [100] iteration[s]. Wavelength: 96.5 μm. The white scale bar in the top-right panel holds for all the diffraction patterns, while the reconstructions share the same black scale bar in (d). All the scale bars equal 2 mm. Adapted with permission from [136].

well as with visible [164] and ultra-violet [168] light and, only recently, it has been demonstrated with THz radiation too [86]. In the next section, the principles of a basic ptychographic algorithm, known as ptychographic iterative engine (PIE) [161], will be outlined.

PIE algorithm: Fig. 8(a) sketches the geometry of a typical ptychographic experiment. We let an aperture crop a coherent beam, referred to as "probe" and represented by the 2D distribution $p(\mathbf{x})$, which impinges on the object with transmission function $o(\mathbf{x})$. A collection of diffraction patterns $I_k(\mathbf{x})$, $k = 1, \ldots, K$, is acquired while shifting the object with respect to the probe by the amounts $\mathbf{x}_k$, such that the regions of the sample illuminated at consecutive positions of the beam partially overlap (typical values of overlap range between 60% and 80% [169]). This over-determination of information allows the reconstruction of $o(\mathbf{x})$ in an iterative fashion.

Provided that the object satisfies the thin object approximation, further discussed in [32,162,170] and also used in the phase retrieval technique described in Section 3.D.3, the wavefront right at the exit of the object plane, referred to as "exit wave" $\psi_k(\mathbf{x})$, can be modeled as the product

$$\psi_k(\mathbf{x}) = p(\mathbf{x}) o_k(\mathbf{x} - \mathbf{x}_k), \tag{21}$$

where the subscript k is used to indicate the kth estimates of the exit wave and the object function. As a rule of thumb, a thickness of up to a few λ guarantees that the thin object approximation is satisfied well enough to yield a resolution comparable to λ. The first step of the PIE algorithm consists of creating an estimate of the exit wave at the detector plane, $\Psi_k(\mathbf{x})$, through a numerical propagation of $\psi_k(\mathbf{x})$ by the object–detector distance d:

$$\Psi_k(\mathbf{x}) = \psi_k(\mathbf{x}) * h_d(\mathbf{x}). \tag{22}$$

Because the amplitude of the wavefront at the detector plane should match the square root of the measured diffraction pattern $I_k(\mathbf{x})$, the "intensity constraint" typical of phase retrieval is applied, yielding the corrected wavefront at the detector plane $\Psi'_k(\mathbf{x})$ [Eq. (24)] and, after a numerical back-propagation, at the object plane $\psi'_k(\mathbf{x})$ [Eq. (24)]:

$$\Psi'_k(\mathbf{x}) = \sqrt{I_k(\mathbf{x})} \frac{\Psi_k(\mathbf{x})}{|\Psi_k(\mathbf{x})|}; \tag{23}$$

$$\psi'_k(\mathbf{x}) = \Psi'_k(\mathbf{x}) * h_{-d}(\mathbf{x}). \tag{24}$$

An update of $o_k(\mathbf{x})$ in the illuminated region, $o_{k+1}(\mathbf{x})$, is calculated through the following:

$$o_{k+1}(\mathbf{x}) = o_k(\mathbf{x}) + \alpha^{(o)} \frac{p_k^*(\mathbf{x} + \mathbf{x}_k)}{\max |p_k(\mathbf{x} + \mathbf{x}_k)|^2} \times [\psi'_k(\mathbf{x} + \mathbf{x}_k) - \psi_k(\mathbf{x} + \mathbf{x}_k)], \tag{25}$$

where $0 < \alpha^{(o)} \leq 1$ tunes the weight of the update. Three derivations of Eq. (25) have been provided in [171]. $o_{k+1}(\mathbf{x})$ is then used in Eq. (21), where the shift $\mathbf{x}_{k+1}$ is used, and the

above procedure repeats, until all the shifts have been used once, which completes one iteration of the algorithm. At the end of each iteration, the convergence of the reconstruction is evaluated through an appropriate error metric so that when the error becomes lower than a predefined threshold, the algorithm terminates.

Some steps of the reconstruction process of a simulated binary Siemens star are displayed in Fig. 8. After using the top left diffraction pattern once, the reconstruction in Figs. 8(b) and 8(c) is obtained. Using all the diffraction patterns yields the reconstruction in Figs. 8(d) and 8(e) after the first iteration. A considerable improvement is obtained after the 100^{th} iteration, especially in the estimation of the phase of the object transmission function [Figs. 8(f) and 8(g)].

Being a phase retrieval technique, ptychography reconstructs the object function by increasing the oversampling ratio with a combination of the two methods listed in Section 3.D. Collecting multiple diffraction patterns, here while translating the object as opposed to typical phase retrieval techniques, where the detector is moved, increases the total number of measured pixels by a factor as high as K and depending on the amount of overlap of the scan. Additionally, the update of the object function is performed only in the illuminated region at each step, which represents a subset of the pixels with unknown value, thus setting a support constraint given by the size of the probe. A comparison between ptychography and the phase retrieval technique presented in Section 3.D.3 is discussed in [36]. Among the numerous studies aiming at reducing the effect of experimental inaccuracies, THz ptychography has benefited from solutions coping with wrong estimates of the probe function [86] and of the shifts [109], which will be reviewed in what follows.

Extended PIE (ePIE) algorithm: the PIE algorithm assumes that the probe function $p(\mathbf{x})$ is known *a priori*, which usually requires its reconstruction by measuring its diffraction pattern without the object.

A closer look at Eq. (21) shows that the probe and the object function could be swapped, with no effect on the computation of the exit wave. In other words, one can conversely regard Eq. (21) as if the object illuminated the probe, and the latter has to be recovered. This suggests that it must be possible to update the reconstruction of the probe alongside that of the object, such that Eq. (21) becomes

$$\psi_k(\mathbf{x}) = p_k(\mathbf{x}) o_k(\mathbf{x} - \mathbf{x}_k), \tag{26}$$

where $p_k(\mathbf{x})$ is the kth estimate of the probe function. Maiden and Rodenburg proposed the ePIE [164] by allowing the probe to be updated in a way analogous to the object, as follows:

$$p_{k+1}(\mathbf{x}) = p_k(\mathbf{x}) + \alpha^{(p)} \frac{o_k^*(\mathbf{x} - \mathbf{x}_k)}{\max |o_k(\mathbf{x} - \mathbf{x}_k)|^2} [\psi_k'(\mathbf{x}) - \psi_k(\mathbf{x})], \tag{27}$$

where the feedback constant for the update of the probe has been indicated with $\alpha^{(p)}$. The algorithm then proceeds like a standard PIE.

Through the ePIE algorithm, Valzania *et al.* reconstructed both amplitude and phase objects, reaching a lateral resolution of about 2λ and a depth resolution of $\lambda/30$ [86], and demonstrated that THz ptychography shares the same intrinsic resolution factors as THz off-axis digital holography [172]. Figure 9 summarizes some reconstruction steps. The imaged object was the nine-spoked Siemens star depicted in Fig. 9(a). Figures 9(b), 9(d), and 9(f) show the diffraction patterns cast

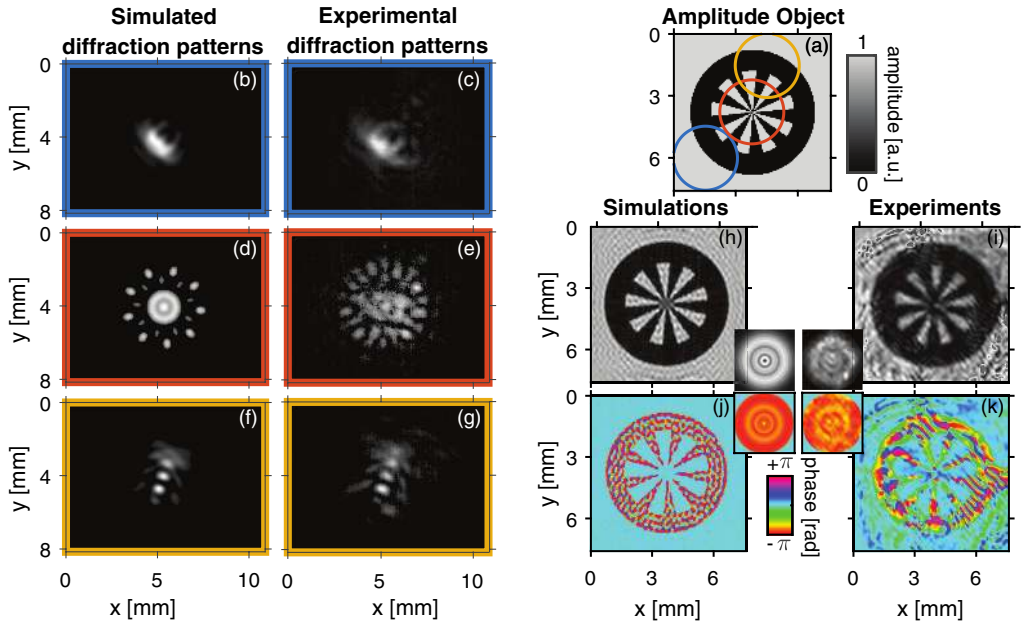

Fig. 9. Ptychographic reconstruction of a pure amplitude object in the shape of a nine-spoked Siemens star, shown in (a). (b), (d), (f), (c), (e), (g) Diffraction patterns obtained by illuminating the simulated [real] object at the positions enclosed by the circles shown in (a) with the corresponding color. (h) , (i) Amplitude and (j) , (k) phase of the reconstructed object. The insets show the reconstructed probes (left column: simulated probe; right column: real probe; top: amplitude; bottom: phase). All the amplitude distributions share the same color bar next to (a), and all the phase distributions share the same color bar between (j) and (k). Adapted with permission from [86] The Optical Society.

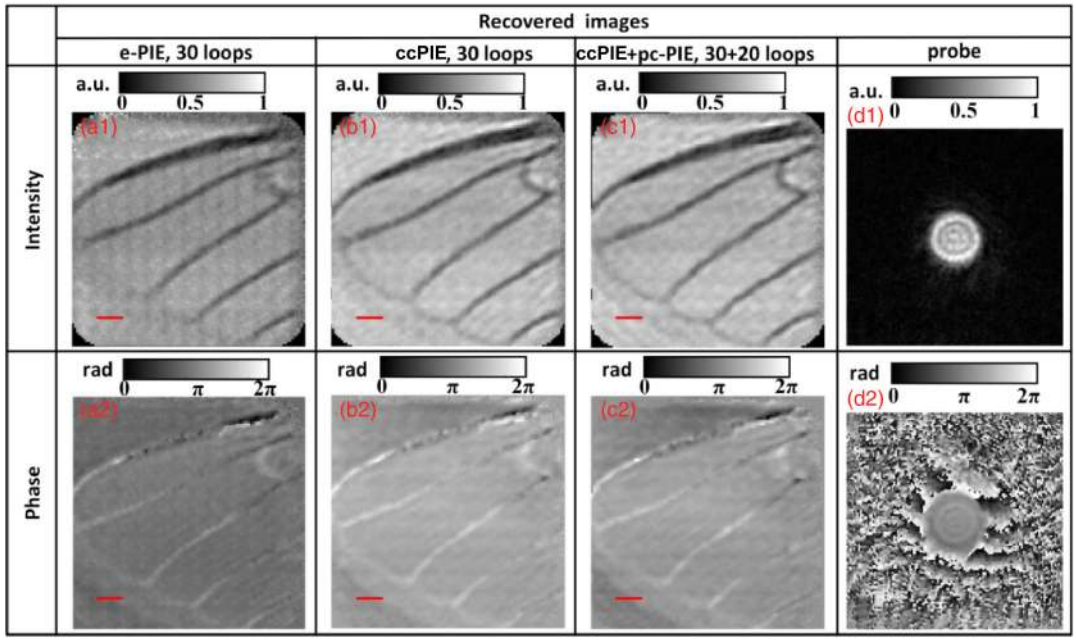

Fig. 10. Intensity (label 1) and phase (label 2) of the ptychographic reconstructions with and without correction of the scan positions. (a) Reconstruction of the object after 30 iterations of the ePIE algorithm and (b) after 30 iterations of the ccPIE algorithm; (c) , (d) reconstruction of the object [probe] after 30 iterations of the ccPIE algorithm and 20 iterations of the pcPIE algorithm. Scale bars: 1 mm. Adapted with permission from [109] The Optical Society.

by a simulated version of the object, when it was illuminated in the regions enclosed by the colored circles in Fig. 9(a), whereas Figs. 9(c), 9(e), and 9(g) contain the corresponding diffraction patterns from a real metallic nine-spoked Siemens star. The reconstructed amplitude and phase from simulated [real] data are shown in Figs. 9(h)–9(k)], respectively. The final estimates of the probe can be found in the nearby insets (simulated probe in the left-hand column and real probe in the right-hand column; amplitude on the top row, phase on the bottom row).

Position-correcting PIE (pcPIE) algorithm: a second source of errors degrading ptychographic reconstructions is the inaccuracy in the knowledge of the shifts. We should expect such inaccuracies to have a considerable effect when they amount to a fraction of the desired lateral resolution. On one hand, this does not pose a problem with THz radiation, as the step resolution of motorized translation stages is currently more than two orders of magnitude smaller than typical THz wavelengths. On the other hand, unwanted angular tilts between the object and the detector plane, which are likely when the object has a maximum thickness of only few λ, introduce uncertainties on the knowledge of the shifts, and should be taken into account even when using THz radiation. For example, assuming shifts $\Delta x = 8\lambda$ [109] applied to an object tilted by $\delta = 7°$ with respect to the detector plane leads to an error in the estimation of the shifts of $\Delta x[1 - \cos(\delta)] \approx \lambda/10$, 20% of the theoretical resolution limit for the lateral resolution, as well as to a wrong reconstruction distance by $\Delta x \sin(\delta) \approx \lambda$.

A "trial and error" algorithm, which can correct the scan positions, was proposed under the name of pcPIE [166]. The algorithm is an extension of the ePIE method, and therefore it is included in an ePIE iteration. The estimate of the exit wave at the object plane, corresponding to the kth diffraction pattern, is computed in a way similar to Eq. (26), however by allowing for a correction $\mathbf{c}_k$ to the nominal shift $\mathbf{x}_k$:

$$\psi_{k0}(\mathbf{x}) = p_k(\mathbf{x}) o_k(\mathbf{x} - (\mathbf{x}_k + \mathbf{c}_k)). \tag{28}$$

At each new iteration, the corrections $\mathbf{c}_k$ are refined by constructing M alternative estimates of ψ_k, denoted with ψ_{km}, $m = 1, 2, \ldots, M$, with M different offsets, randomly chosen within a distance c from the starting position at $\mathbf{x}_k + \mathbf{c}_k$, as follows:

$$\psi_{km}(\mathbf{x}) = p_k(\mathbf{x}) o_k(\mathbf{x} - (\mathbf{x}_k + \mathbf{c}_k + c\,\mathbf{\Delta}_m)), \tag{29}$$

where both components of $\mathbf{\Delta}_m$ are selected from a uniform probability distribution within the range $[-1, 1]$. Equations (28) and (29) make up a set of estimates for ψ_k, which are propagated to the detector plane, i.e.,

$$\Psi_{kn}(\mathbf{x}) = \psi_{kn}(\mathbf{x}) * h_d(\mathbf{x}),\ n = 0, 1, \ldots, M, \tag{30}$$

and evaluated again using an appropriate error metric. The estimate of the wavefront at the detector plane leading to the minimum error, denoted with $\Psi_{kn'}(\mathbf{x})$, is then modified according to the intensity constraint and back-propagated to the object plane, as in Eqs. (23) and (24). If the selected wavefront belongs to the set of newly tried wavefronts, i.e., $n' > 0$, the value of $\mathbf{c}_k$ is replaced by $\mathbf{c}_k + c\,\mathbf{\Delta}_{n'}$; otherwise, it is kept unchanged. The algorithm proceeds with the next scan position, and after all of them have been used, a new iteration starts, when a lower value of c is employed.

Cross-correlation-based PIE (ccPIE) algorithm: alternative solutions to correct the scan positions were proposed, using cross-correlation on the estimates of the object at consecutive iterations [173], or at consecutive scan positions [174]. Rong

et al. [109] have recently proposed a similar method, here referred to as ccPIE, which retrieves the shifts through a cross-correlation directly performed on the exit waves at the object plane, and they demonstrated its principle with a THz laser. In a standard ePIE framework, they suggested refining the shifts after correcting the exit wave with the intensity constraint, i.e.,

$$\mathbf{x}_k \equiv \arg\max_{\xi}[\psi'_k(\mathbf{x}) \star \psi_1(\mathbf{x})](\boldsymbol{\xi}), \tag{31}$$

where $\star$ denotes cross-correlation. Their method was applied to the reconstruction of a cicadas' forewing. Owing to its thickness of about 10 μm, tilts between the object plane and the detector plane are inevitable. The ccPIE algorithm improved the reconstruction [Figs. 10(b1) and 10(b2)], compared to when only the ePIE algorithm was applied [Figs. 10(a1) and 10(a2)]. The improvements after refining the scan positions through 20 additional iterations of pcPIE [Figs. 10(c1) and 10(c2)] are more subtle.

4. CONCLUSION AND OUTLOOK

In conclusion, we have reviewed the state of the research on THz coherent lensless imaging, focusing on the tools currently available for its implementation, their combination in successful imaging setups, and image reconstruction techniques.

Several coherent THz sources allow coherent THz imaging. Gas lasers have not seen any development in the last decades; their output will remain limited by the gas volume and by the cavity size. QCLs are developing rapidly and deliver ever-higher power. Future development will be directed towards relaxed cooling conditions, eventually operating at room temperature. There is a limitation to photo mixing, even when non-linear materials are getting more and more effective, as two pump photons are needed to create one THz photon of a fraction of the energy. An improvement in photomixing THz sources could be found in array geometries, which would allow combining the output of several device elements or large area emitters. With proper control, the emission wave overlay can also be achieved in a coherent way.

The state-of-the-art detectors for lensless imaging in the 1–4 THz range are microbolometers and pyroelectric cameras. Due to the lack of high-resolution cameras in the sub-THz range, lensless imaging is still realized by scanning single-pixel detectors.

Three directions can be identified towards the future development of THz cameras for lensless imaging. The first one aims at higher resolution, by increasing the array size to values comparable to those of infrared microbolometer arrays. Note that for THz applications, using wavelengths of 100 μm and above, pixels much smaller than the wavelength are already available, and decreasing their size is not expected to crucially impact the imaging performance. The second direction points towards low-cost infrared cameras, whose small detector areas could be compensated for by synthetic aperture methods, controlled by smartphones [175]. The third direction is seeking for efficient area detectors in the sub-THz regime. Commercial area detectors with 64×64 pixels with a pitch of 1.5 mm are available [176], based on photon detector technology. They have already been employed in THz imaging studies for security and non-destructive testing applications, and represent good candidates for sub-THz coherent lensless imaging. An alternative has been proposed using a THz microbolometer camera, highly sensitive at sub-THz frequencies, in combination with specifically designed THz objectives for a larger field of view [177]. Such a solution is also applicable to digital holography with ingenious reference beam injection techniques, as shown in [178].

We have reviewed the digital holographic and phase retrieval techniques already implemented with THz radiation. Basically, they share the same principles as the corresponding implementations at shorter wavelengths, among which is the fact that the lateral resolution is diffraction limited. However, we have shown that in a typical THz imaging experiment, the conditions for the far-field approximation, commonly employed with visible light and x rays, are not met. It is therefore necessary to replace the Fourier transform with the Rayleigh–Sommerfeld integral (or, equivalently, the angular spectrum approach) to numerically propagate complex wavefronts.

THz off-axis digital holography was the first variant of holography demonstrated with a coherent THz source, owing to two reasons. First, it can be performed with large enough off-axis angles to separate the diffraction orders in the Fourier spectrum of the hologram, without the risk of undersampling by the detector pixels. Second, both transmission and reflection modes are allowed. The latter geometry makes it particularly appealing for imaging-absorbing objects as well.

On the contrary, in-line digital holography is based on the assumption that part of the incident beam is not diffracted by the object, which thus must be probed in transmission and smaller than the beam size or weakly absorbing. This is the case for, e.g., excised biological tissue slices, with a thickness much lower than the wavelength, which were successfully reconstructed with THz radiation. The main advantage of in-line digital holography consists of the possibility to shorten the reconstruction distance, thereby improving the resolution compared to off-axis digital holography. The compact experimental setup comes at the expense of the twin image problem. In order to cope with it, the analysis of in-line digital holograms borrowed several solutions from another category of coherent lensless imaging techniques, namely, phase retrieval.

Phase retrieval imaging techniques reconstruct the object starting from a guessed solution and improving it by imposing a support constraint or intensity constraints from a set of diffraction patterns recorded at different object–detector distances.

Ptychography, combining typical iterative phase retrieval algorithms with a setup inherited from scanning microscopy, has also been recently migrated from electron imaging, where it was originally conceived, to the THz range, and was shown to be a valuable alternative to the widespread THz off-axis digital holography. Taking advantage of the numerous ptychographic algorithms and implementations already demonstrated will make THz ptychography a powerful tool and approach it to real-life applications. For example, THz ptychography in reflection [179] would allow imaging *in vivo* biological samples, while a multi-slice implementation [180] would deliver coherent tomographic reconstructions without either rotating the sample, or using an interferometric approach.

In the same way as for the imaging techniques, migrating optical components to the THz range would drastically expand the capabilities of THz imaging. For instance, THz spatial light modulators (THz-SLMs) would pave the way for THz wavefront shaping [181]. THz imaging could thus benefit from the plethora of achievements obtained in biomedical optics with visible light. Crucially, this will allow using structured illumination techniques to improve the resolution [182] and imaging through multiple-scattering media [183], which can be successfully exploited in non-destructive industrial inspection with THz waves. Despite different prototypes of THz-SLMs having been demonstrated and reported in Refs. [12,13], they are far from their counterparts in the visible range.

Although this review makes it clear that THz imaging owes a lot to imaging with electrons, x rays, and visible light, we should not forget that new coherent lensless imaging techniques are being developed in the THz range, with the potential to be implemented at different wavelengths, too. In particular, we have described an innovative phase retrieval technique for imaging through a moving and scattering barrier, whose loose assumptions make it applicable wherever imaging hidden objects is an issue. Along this line, we expect that the essential role of THz radiation for today's scientific and technological advancements will spur the THz imaging community to develop further coherent lensless imaging techniques that will prove beneficial for diverse applications and wavelength ranges.

For these reasons, we foresee a flourishing era at the interface between THz science and coherent lensless imaging techniques.

Funding. Schweizerischer Nationalfonds zur Förderung der Wissenschaftlichen Forschung (200021_160078/1); European Regional Development Fund; National Natural Science Foundation of China (61675010); Beijing Nova Program (xx2018072).

Disclosures. The authors declare that there are no conflicts of interest related to this paper.

[†]These authors equally contributed to this work.

REFERENCES

1. S. S. Dhillon, M. S. Vitiello, E. H. Linfield, A. G. Davies, M. C. Hoffmann, J. Booske, C. Paoloni, M. Gensch, P. Weightman, G. P. Williams, E. Castro-Camus, D. R. S. Cumming, F. Simoens, I. Escorcia-Carranza, J. Grant, S. Lucyszyn, M. Kuwata-Gonokami, K. Konishi, M. Koch, C. A. Schmuttenmaer, T. L. Cocker, R. Huber, A. G. Markelz, Z. D. Taylor, V. P. Wallace, J. A. Zeitler, J. Sibik, T. M. Korter, B. Ellison, S. Rea, P. Goldsmith, K. B. Cooper, R. Appleby, D. Pardo, P. G. Huggard, V. Krozer, H. Shams, M. Fice, C. Renaud, A. Seeds, A. Stöhr, M. Naftaly, N. Ridler, R. Clarke, J. E. Cunningham, and M. B. Johnston, "The 2017 terahertz science and technology roadmap," J. Phys. D **50**, 043001 (2017).
2. M. Koch, S. Hunsche, P. Schumacher, M. Nuss, J. Feldmann, and J. Fromm, "THz-imaging: a new method for density mapping of wood," Wood Sci. Technol. **32**, 421–427 (1998).
3. R. Piesiewicz, C. Jansen, S. Wietzke, D. Mittleman, M. Koch, and T. Kürner, "Properties of building and plastic materials in the THz range," Int. J. Infrared Millim. Waves **28**, 363–371 (2007).
4. P. Zolliker, M. Rüggeberg, L. Valzania, and E. Hack, "Extracting wood properties from structured THz spectra: birefringence and water content," IEEE Trans. Terahertz Sci. Technol. **7**, 722–731 (2017).
5. J. Wang, J. Zhang, T. Chang, L. Liu, and H.-L. Cui, "Terahertz nondestructive imaging for foreign object detection in glass fibre-reinforced polymer composite panels," Infrared Phys. Technol. **98**, 36–44 (2019).
6. J. Dai, J. Zhang, W. Zhang, and D. Grischkowsky, "Terahertz time-domain spectroscopy characterization of the far-infrared absorption and index of refraction of high-resistivity, float-zone silicon," J. Opt. Soc. Am. B **21**, 1379–1386 (2004).
7. A. Redo-Sanchez, B. Heshmat, A. Aghasi, S. Naqvi, M. Zhang, J. Romberg, and R. Raskar, "Terahertz time-gated spectral imaging for content extraction through layered structures," Nat. Commun. **7**, 12665 (2016).
8. É. Hérault, M. Hofman, F. Garet, and J.-L. Coutaz, "Observation of terahertz beam diffraction by fabrics," Opt. Lett. **38**, 2708–2710 (2013).
9. A. Redo-Sanchez, N. Laman, B. Schulkin, and T. Tongue, "Review of terahertz technology readiness assessment and applications," J. Infrared Millim. Terahertz Waves **34**, 500–518 (2013).
10. Y. He, P. I. Ku, J. Knab, J. Chen, and A. Markelz, "Protein dynamical transition does not require protein structure," Phys. Rev. Lett. **101**, 178103 (2008).
11. S. Leinß, T. Kampfrath, K. V. Volkmann, M. Wolf, J. T. Steiner, M. Kira, S. W. Koch, A. Leitenstorfer, and R. Huber, "Terahertz coherent control of optically dark paraexcitons in Cu_2O," Phys. Rev. Lett. **101**, 246401 (2008).
12. D. M. Mittleman, "Twenty years of terahertz imaging," Opt. Express **26**, 9417–9431 (2018).
13. H. Guerboukha, K. Nallappan, and M. Skorobogatiy, "Toward real-time terahertz imaging," Adv. Opt. Photon. **10**, 843–938 (2018).
14. C. Fattinger and D. Grischkowsky, "Point source terahertz optics," Appl. Phys. Lett. **53**, 1480–1482 (1988).
15. M. C. Nuss and J. Orenstein, "Terahertz time-domain spectroscopy," in *Millimeter and Submillimeter Wave Spectroscopy of Solids* (Springer, 1998), pp. 7–50.
16. R. K. May, M. J. Evans, S. Zhong, I. Warr, L. F. Gladden, Y. Shen, and J. A. Zeitler, "Terahertz in-line sensor for direct coating thickness measurement of individual tablets during film coating in real-time," J. Pharm. Sci. **100**, 1535–1544 (2011).
17. D. M. Mackenzie, P. R. Whelan, P. Bøggild, P. U. Jepsen, A. Redo-Sanchez, D. Etayo, N. Fabricius, and D. H. Petersen, "Quality assessment of terahertz time-domain spectroscopy transmission and reflection modes for graphene conductivity mapping," Opt. Express **26**, 9220–9229 (2018).
18. P. Bøggild, D. M. Mackenzie, P. R. Whelan, D. H. Petersen, J. D. Buron, A. Zurutuza, J. Gallop, L. Hao, and P. U. Jepsen, "Mapping the electrical properties of large-area graphene," 2D Mater. **4**, 042003 (2017).
19. A. Bitzer, H. Merbold, A. Thoman, T. Feurer, H. Helm, and M. Walther, "Terahertz near-field imaging of electric and magnetic resonances of a planar metamaterial," Opt. Express **17**, 3826–3834 (2009).
20. T. L. Cocker, V. Jelic, M. Gupta, S. J. Molesky, J. A. Burgess, G. De Los Reyes, L. V. Titova, Y. Y. Tsui, M. R. Freeman, and F. A. Hegmann, "An ultrafast terahertz scanning tunnelling microscope," Nat. Photonics **7**, 620–625 (2013).
21. W. Withayachumnankul and M. Naftaly, "Fundamentals of measurement in terahertz time-domain spectroscopy," J. Infrared Millim. Terahertz Waves **35**, 610–637 (2014).
22. N. V. Petrov, M. S. Kulya, A. N. Tsypkin, V. G. Bespalov, and A. Gorodetsky, "Application of terahertz pulse time-domain holography for phase imaging," IEEE Trans. Terahertz Sci. Technol. **6**, 464–472 (2016).
23. Y. L. Lim, K. Bertling, T. Taimre, T. Gillespie, C. Glenn, A. Robinson, D. Indjin, Y. Han, L. Li, E. H. Linfield, A. G. Davies, P. Dean, and A. D. Rakić, "Coherent imaging using laser feedback interferometry with pulsed-mode terahertz quantum cascade lasers," Opt. Express **27**, 10221–10233 (2019).

24. J. P. Guillet, B. Recur, L. Frederique, B. Bousquet, L. Canioni, I. Manek-Hönninger, P. Desbarats, and P. Mounaix, "Review of terahertz tomography techniques," J. Infrared Millim. Terahertz Waves **35**, 382–411 (2014).
25. M. Suga, Y. Sasaki, T. Sasahara, T. Yuasa, and C. Otani, "THz phase-contrast computed tomography based on Mach-Zehnder interferometer using continuous-wave source: proof of the concept," Opt. Express **21**, 25389–25402 (2013).
26. M. Heimbeck, D. Marks, D. Brady, and H. Everitt, "Terahertz interferometric synthetic aperture tomography for confocal imaging systems," Opt. Lett. **37**, 1316–1318 (2012).
27. E. J. Candès and M. B. Wakin, "An introduction to compressive sampling [a sensing/sampling paradigm that goes against the common knowledge in data acquisition]," IEEE Signal Process. Mag. **25**(2), 21–30 (2008).
28. W. L. Chan, K. Charan, D. Takhar, K. F. Kelly, R. G. Baraniuk, and D. M. Mittleman, "A single-pixel terahertz imaging system based on compressed sensing," Appl. Phys. Lett. **93**, 121105 (2008).
29. W. L. Chan, M. L. Moravec, R. G. Baraniuk, and D. M. Mittleman, "Terahertz imaging with compressed sensing and phase retrieval," Opt. Lett. **33**, 974–976 (2008).
30. M. Guizar-Sicairos, *Methods for Coherent Lensless Imaging and X-Ray Wavefront Measurement* (University of Rochester, 2010).
31. J. R. Fienup, "Phase retrieval algorithms: a comparison," Appl. Opt. **21**, 2758–2769 (1982).
32. J. M. Rodenburg, "Ptychography and related diffractive imaging methods," Adv. Imaging Electron Phys. **150**, 87–184 (2008).
33. T. Kreis, *Handbook of Holographic Interferometry: Optical and Digital Methods* (Wiley, 2006).
34. K.-E. Peiponen, A. Zeitler, and M. Kuwata-Gonokami, *Terahertz Spectroscopy and Imaging* (Springer, 2012), Vol. **171**.
35. L. Valzania, P. Zolliker, and E. Hack, "Topography of hidden objects using THz digital holography with multi-beam interferences," Opt. Express **25**, 11038–11047 (2017).
36. L. Valzania, P. Zolliker, and E. Hack, "Coherent reconstruction of a textile and a hidden object with terahertz radiation," Optica **6**, 518–523 (2019).
37. G. P. Gallerano and S. Biedron, "Overview of terahertz radiation sources," in *Proceedings of the Free Electron Laser Conference (FEL)* (2004), Vol. **1**, pp. 216–221.
38. J. R. Freeman, H. E. Beere, and D. A. Ritchie, "Generation and detection of terahertz radiation," in *Terahertz Spectroscopy and Imaging*, K.-E. Peiponen, A. Zeitler, and M. Kuwata-Gonokami, eds. (Springer, 2012), pp. 1–28.
39. F. Sizov, "Terahertz radiation detectors: the state-of-the-art," Semicond. Sci. Technol. **33**, 123001 (2018).
40. A. Rogalski, *Infrared and Terahertz Detectors* (CRC Press, 2018).
41. A. Crocker, H. A. Gebbie, M. F. Kimmitt, and L. E. S. Mathias, "Stimulated emission in the far infra-red," Nature **201**, 250–251 (1964).
42. M. Naftaly, *Terahertz Metrology* (Artech House, 2015).
43. H. Minamide and H. Ito, "Frequency-agile terahertz-wave generation and detection using a nonlinear optical conversion, and their applications for imaging," C. R. Phys. **11**, 457–471 (2010).
44. S. Preu, G. H. Dohler, S. Malzer, L. J. Wang, and A. C. Gossard, "Tunable, continuous-wave terahertz photomixer sources and applications," J. Appl. Phys. **109**, 061301 (2011).
45. Y. J. Ding, "Progress in terahertz sources based on difference-frequency generation," J. Opt. Soc. Am. B **31**, 2696–2711 (2014).
46. F. D. J. Brunner, S. H. Lee, O. P. Kwon, and T. Feurer, "THz generation by optical rectification of near-infrared laser pulses in the organic nonlinear optical crystal HMQ-TMS," Opt. Mater. Express **4**, 1586–1592 (2014).
47. M. Jazbinsek, U. Puc, A. Abina, and A. Zidansek, "Organic crystals for THz photonics," Appl. Sci. **9**, 882 (2019).
48. X. Xie, J. M. Dai, and X. C. Zhang, "Coherent control of THz wave generation in ambient air," Phys. Rev. Lett. **96**, 075005 (2006).
49. X.-C. Zhang and J. Xu, *Introduction to THz Wave Photonics* (Springer, 2010).
50. I. Park, "Investigations of the generation of tunable continuous-wave terahertz radiation and its spectroscopic applications," Ph. D. thesis (Technische Universität Darmstadt, 2007).
51. J. Faist, F. Capasso, D. L. Sivco, C. Sirtori, A. L. Hutchinson, and A. Y. Cho, "Quantum cascade laser," Science **264**, 553–556 (1994).
52. M. Rochat, L. Ajili, H. Willenberg, J. Faist, H. Beere, G. Davies, E. Linfield, and D. Ritchie, "Low-threshold terahertz quantum-cascade lasers," Appl. Phys. Lett. **81**, 1381–1383 (2002).
53. S. Kumar, "Recent progress in terahertz quantum cascade lasers," IEEE J. Sel. Top. Quantum Electron. **17**, 38–47 (2011).
54. X. M. Wang, C. L. Shen, T. Jiang, Z. Q. Zhan, Q. H. Deng, W. H. Li, W. D. Wu, N. Yang, W. D. Chu, and S. Q. Duan, "High-power terahertz quantum cascade lasers with similar to 0.23 W in continuous-wave mode," AIP Adv. **6**, 075210 (2016).
55. B. S. Williams, "Terahertz quantum-cascade lasers," Nat. Photonics **1**, 517–525 (2007).
56. J. Faist, G. Scalari, M. Fischer, and M. Beck, "Terahertz quantum cascade lasers: 10 years of active region and material progresses," in *International Conference on Infrared, Millimeter, and Terahertz Waves* (2011), pp. 1–2.
57. M. A. Belkin and F. Capasso, "New frontiers in quantum cascade lasers: high performance room temperature terahertz sources," Phys. Scripta **90**, 118002 (2015).
58. S. Y. Jung, Y. F. Jiang, K. Vijayraghavan, A. T. Jiang, F. Demmerle, G. Boehm, X. J. Wang, M. Troccoli, M. C. Amann, and M. A. Belkin, "Recent progress in widely tunable single-mode room temperature terahertz quantum cascade laser sources," IEEE J. Sel. Top. Quantum Electron. **21**, 134–143 (2015).
59. Y. Jin, L. Gao, J. Chen, C. Z. Wu, J. L. Reno, and S. Kumar, "High power surface emitting terahertz laser with hybrid second- and fourth-order Bragg gratings," Nat. Commun. **9**, 1407 (2018).
60. L. Mahler, A. Tredicucci, and M. S. Vitiello, "Quantum cascade laser: a compact, low cost, solid-state source for plasma diagnostics," J. Instrum. **7**, C02018 (2012).
61. A. A. Danylov, T. M. Goyette, J. Waldman, M. J. Coulombe, A. J. Gatesman, R. H. Giles, X. F. Qian, N. Chandrayan, S. Vangala, K. Termkoa, W. D. Goodhue, and W. E. Nixon, "Coherent imaging at 2.4 THz with a CW quantum cascade laser transmitter," Proc. SPIE **7601**, 760105 (2010).
62. O. A. Klimenko, Y. A. Mityagin, S. A. Savinov, V. N. Murzin, N. V. Dyakonova, P. Solignac, and W. Knap, "Terahertz wide range tunable cyclotron resonance p-Ge laser," 16th International Conference on Electron Dynamics in Semiconductors, Optoelectronics and Nanostructures (Edison 16) (2009), Vol. **193**.
63. E. Starikov, P. Shiktorov, and V. Gruzinskis, "Physical mechanisms for terahertz generation," in *Ultrafast Phenomena in Semiconductors* (1999), Vol. **297-2**, 271–278.
64. Z. S. Gribnikov, R. R. Bashirov, and V. V. Mitin, "Negative effective mass mechanism of negative differential drift velocity and terahertz generation," IEEE J. Sel. Top. Quantum Electron. **7**, 630–640 (2001).
65. A. Maestrini, B. Thomas, H. Wang, C. Jung, J. Treuttel, Y. Jin, G. Chattopadhyay, I. Mehdi, and G. Beaudin, "Schottky diode-based terahertz frequency multipliers and mixers," C. R. Phys. **11**, 480–495 (2010).
66. A. Dobroiu, M. Yamashita, Y. N. Ohshima, Y. Morita, C. Otani, and K. Kawase, "Terahertz imaging system based on a backward-wave oscillator," Appl. Opt. **43**, 5637–5646 (2004).
67. S. Martens, B. Gompf, and M. Dressel, "Characterization of continuous-wave terahertz sources: laser mixing versus backward-wave oscillators," Appl. Opt. **48**, 5490–5496 (2009).
68. D. Fast, W. Hurlbut, and V. G. Kozlov, "Extending spectral coverage of BWOs combined with frequency multipliers to 2.6 THz," Proc. SPIE **8261**, 82610L (2012).
69. C.-W. Baik, Y.-M. Son, S. I. Kim, S. C. Jun, J.-S. Kim, J. Hwang, J.-M. Kim, S.-W. Moon, H. J. Kim, J.-K. So, and P. Gun-Sik, "Microfabricated coupled-cavity backward-wave oscillator for terahertz imaging," in *IEEE International Vacuum Electronics Conference* (2008), pp. 398–399.
70. H. J. Cha, Y. U. Jeong, S. H. Park, B. C. Lee, and S. H. Park, "Power spectrum and coherence length measurements of a compact terahertz free-electron laser," J. Korean Phys. Soc. **47**, 798–802 (2005).

71. J. H. Booske, R. J. Dobbs, C. D. Joye, C. L. Kory, G. R. Neil, G. S. Park, J. Park, and R. J. Temkin, "Vacuum electronic high power terahertz sources," IEEE Trans. Terahertz Sci. Technol. **1**, 54–75 (2011).
72. V. S. Cherkassky, B. A. Knyazev, S. V. Kozlov, V. V. Kubarev, G. N. Kulipanov, A. N. Matveenko, V. M. Popik, D. N. Root, P. D. Rudych, O. A. Shevchenko, A. V. Trifutina, and N. A. Vinokurov, "Terahertz imaging and holography with a high-power free electron laser," in *Joint 30th International Conference on Infrared and Millimeter Waves and 13th International Conference on Terahertz Electronics* (2005), Vol. **2**, pp. 337–338.
73. V. Cherkassky, B. Knyazev, V. Kubarev, G. Kulipanov, G. Kuryshev, A. Matveenko, A. Petrov, V. Popik, M. Scheglov, O. Shevchenko, and N. Vinokurov, "Imaging techniques for a high-power THz free electron laser," Nucl. Instrum. Methods Phys. Res. A **543**, 102–109 (2005).
74. Y. U. Jeong, G. M. Kazakevitch, H. J. Cha, S. H. Park, and B. C. Lee, "Application of a wide-band compact FEL on THz imaging," Nucl. Instrum. Methods Phys. Res. A **543**, 90–95 (2005).
75. Y. Y. Choporova, B. A. Knyazev, and M. S. Mitkov, "Classical holography in the terahertz range: recording and reconstruction techniques," IEEE Trans. Terahertz Sci. Technol. **5**, 836–844 (2015).
76. B. Knyazev, M. Dem'yanenko, and D. Esaev, "Terahertz imaging with a 160 × 120 pixel microbolometer 90-fps camera," in *Joint 32nd International Conference on Infrared and Millimeter Waves and the 15th International Conference on Terahertz Electronics* (IEEE, 2007), pp. 360–361.
77. B. N. Behnken, G. Karunasiri, D. R. Chamberlin, P. R. Robrish, and J. Faist, "Real-time imaging using a 2.8 THz quantum cascade laser and uncooled infrared microbolometer camera," Opt. Lett. **33**, 440–442 (2008).
78. B. N. Behnken, M. Lowe, G. Karunasiri, D. Chamberlain, P. Robrish, and J. Faist, "Detection of 3.4 THz radiation from a quantum cascade laser using a microbolometer infrared camera," Proc. SPIE **6549**, 65490C (2007).
79. "Ophir THz laser measurement products," 2019, https://bit.ly/2xW12Ex.
80. L. Le Noc, B. Tremblay, A. Martel, C. Chevalier, N. Blanchard, M. Morissette, L. Mercier, F. Duchesne, L. Gagnon, P. Couture, F. Lévesque, N. Desnoyers, M. Demers, F. Lamontage, H. Jerominek, and A. Bergeron, "1280 × 960 pixel microscanned infrared imaging module," Proc. SPIE **7660**, 766021 (2010).
81. M. Georges, "Long-wave infrared digital holography," in *New Techniques in Digital Holography* (2015), pp. 219–254.
82. E. Hack, L. Valzania, G. Gäumann, M. Shalaby, C. P. Hauri, and P. Zolliker, "Comparison of thermal detector arrays for off-axis THz holography and real-time THz imaging," Sensors **16**, 221 (2016).
83. E. Hack and P. Zolliker, "Terahertz holography for imaging amplitude and phase objects," Opt. Express **22**, 16079–16086 (2014).
84. P. Zolliker and E. Hack, "THz holography in reflection using a high resolution microbolometer array," Opt. Express **23**, 10957–10967 (2015).
85. M. Locatelli, M. Ravaro, S. Bartalini, L. Consolino, M. S. Vitiello, R. Cicchi, F. Pavone, and P. De Natale, "Real-time terahertz digital holography with a quantum cascade laser," Sci. Rep. **5**, 13566 (2015).
86. L. Valzania, T. Feurer, P. Zolliker, and E. Hack, "Terahertz ptychography," Opt. Lett. **43**, 543–546 (2018).
87. Z. Li, Q. Yan, Y. Qin, W. Kong, G. Li, M. Zou, D. Wang, Z. You, and X. Zhou, "Sparsity-based continuous-wave terahertz lens-free on-chip holography with sub-wavelength resolution," Opt. Express **27**, 702–713 (2019).
88. N. Oda, "Uncooled bolometer-type terahertz focal plane array and camera for real-time imaging," C. R. Phys. **11**, 496–509 (2010).
89. M. Dem'yanenko, D. Esaev, V. Ovsyuk, B. Fomin, A. Aseev, B. Knyazev, G. Kulipanov, and N. Vinokurov, "Microbolometer detector arrays for the infrared and terahertz ranges," J. Opt. Technol. **76**, 739–743 (2009).
90. D. Dufour, L. Marchese, M. Terroux, H. Oulachgar, F. Généreux, M. Doucet, L. Mercier, B. Tremblay, C. Alain, P. Beaupré, N. Blanchard, M. Bolduc, C. Chevalier, D. D'Amato, Y. Desroches, F. Duchesne, L. Gagnon, S. Ilias, H. Jerominek, F. Lagacé, J. Lambert, F. Lamontagne, L. Le Noc, A. Martel, O. Pancrati, J.-E. Paultre, T. Pope, F. Provençal, P. Topart, C. Vachon, S. Verreault, and A. Bergeron," Review of terahertz technology development at INO," J. Infrared Millim. Terahertz Wavesc **36**, 922–946 (2015).
91. N. Oda, S. Kurashina, M. Miyoshi, K. Doi, T. Ishi, T. Sudou, T. Morimoto, H. Goto, and T. Sasaki, "Microbolometer terahertz focal plane array and camera with improved sensitivity in the sub-terahertz region," J. Infrared Millim. Terahertz Waves **36**, 947–960 (2015).
92. J. Oden, J. Meilhan, J. Lalanne-Dera, J.-F. Roux, F. Garet, J.-L. Coutaz, and F. Simoens, "Imaging of broadband terahertz beams using an array of antenna-coupled microbolometers operating at room temperature," Opt. Express **21**, 4817–4825 (2013).
93. F. Simoens, J. Meilhan, S. Gidon, G. Lasfargues, J. L. Dera, J. L. Ouvrier-Buffet, S. Pocas, W. Rabaud, F. Guellec, B. Dupont, S. Martin, and A. C. Simon, "Antenna-coupled microbolometer based uncooled 2D array and camera for 2D real-time terahertz imaging," Proc. SPIE **8846**, 88460O (2013).
94. M. Sakhno, A. Golenkov, and F. Sizov, "Uncooled detector challenges: millimeter-wave and terahertz long channel field effect transistor and Schottky barrier diode detectors," J. Appl. Phys. **114**, 164503 (2013).
95. W. Knap and M. Dyakonov, "Field effect transistors for terahertz applications," in *Handbook of Terahertz Technology for Imaging, Sensing and Communications* (Elsevier, 2013), pp. 121–155.
96. N. Dyakonova, D. Coquillat, F. Teppe, W. Knap, J. Suszek, A. Siemion, M. Sypek, D. B. But, P. Sai, I. Yahniuk, G. Cywinski, J. Marczewski, M. Zaborowski, D. Tomaszewski, and P. Zagrajek, "Terahertz vision using field effect transistors detectors arrays," in *22nd International Microwave and Radar Conference (MIKON)* (2018), pp. 711–714.
97. R. Han, Y. Zhang, Y. Kim, D. Y. Kim, H. Shichijo, E. Afshari, and K. O. Kenneth, "Active terahertz imaging using Schottky diodes in CMOS: array and 860-GHz pixel," IEEE J. Solid-State Circuits **48**, 2296–2308 (2013).
98. A. J. Gatesman, A. Danylov, T. M. Goyette, J. C. Dickinson, R. H. Giles, W. Goodhue, J. Waldman, W. E. Nixon, and W. Hoen, "Terahertz behavior of optical components and common materials," Proc. SPIE **6212**, 62120E (2006).
99. M. C. Kemp, "Explosives detection by terahertz spectroscopy—a bridge too far?" IEEE Trans. Terahertz Sci. Technol. **1**, 282–292 (2011).
100. M. S. Heimbeck, W. R. Ng, D. R. Golish, M. E. Gehm, and H. O. Everitt, "Terahertz digital holographic imaging of voids within visibly opaque dielectrics," IEEE Trans. Terahertz Sci. Technol. **5**, 110–116 (2015).
101. M. Naftaly and R. E. Miles, "Terahertz time-domain spectroscopy for material characterization," Proc. IEEE **95**, 1658–1665 (2007).
102. Y.-S. Jin, G.-J. Kim, and S.-G. Jeon, "Terahertz dielectric properties of polymers," J. Korean Phys. Soc. **49**, 513–517 (2006).
103. J. Bjarnason, T. Chan, A. Lee, M. Celis, and E. Brown, "Millimeter-wave, terahertz, and mid-infrared transmission through common clothing," Appl. Phys. Lett. **85**, 519–521 (2004).
104. T. Bowman, Y. Wu, J. Gauch, L. K. Campbell, and M. El-Shenawee, "Terahertz imaging of three-dimensional dehydrated breast cancer tumors," J. Infrared Millim. Terahertz Waves **38**, 766–786 (2017).
105. S.-H. Ding, Q. Li, Y.-D. Li, and Q. Wang, "Continuous-wave terahertz digital holography by use of a pyroelectric array camera," Opt. Lett. **36**, 1993–1995 (2011).
106. L. Rong, T. Latychevskaia, D. Wang, X. Zhou, H. Huang, Z. Li, and Y. Wang, "Terahertz in-line digital holography of dragonfly hindwing: amplitude and phase reconstruction at enhanced resolution by extrapolation," Opt. Express **22**, 17236–17245 (2014).
107. M. Wan, I. Muniraj, R. Malallah, L. Zhao, J. P. Ryle, L. Rong, J. J. Healy, D. Wang, and J. T. Sheridan, "Sparsity based terahertz reflective off-axis digital holography," Proc. SPIE **10233**, 102330T (2017).
108. L. Rong, T. Latychevskaia, C. Chen, D. Wang, Z. Yu, X. Zhou, Z. Li, H. Huang, Y. Wang, and Z. Zhou, "Terahertz in-line digital holography of human hepatocellular carcinoma tissue," Sci. Rep. **5**, 8445 (2015).

109. L. Rong, C. Tang, D. Wang, B. Li, F. Tan, Y. Wang, and X. Shi, "Probe position correction based on overlapped object wavefront cross-correlation for continuous-wave terahertz ptychography," Opt. Express **27**, 938–950 (2019).
110. H. Huang, L. Rong, D. Wang, W. Li, Q. Deng, B. Li, Y. Wang, Z. Zhan, X. Wang, and W. Wu, "Synthetic aperture in terahertz in-line digital holography for resolution enhancement," Appl. Opt. **55**, A43–A48 (2016).
111. Q. Deng, W. Li, X. Wang, Z. Li, H. Huang, C. Shen, Z. Zhan, R. Zou, T. Jiang, and W. Wu, "High-resolution terahertz inline digital holography based on quantum cascade laser," Opt. Eng. **56**, 113102 (2017).
112. M. Yamagiwa, T. Ogawa, T. Minamikawa, D. G. Abdelsalam, K. Okabe, N. Tsurumachi, Y. Mizutani, T. Iwata, H. Yamamoto, and T. Yasui, "Real-time amplitude and phase imaging of optically opaque objects by combining full-field off-axis terahertz digital holography with angular spectrum reconstruction," J. Infrared Millim. Terahertz Waves **39**, 561–572 (2018).
113. T. Jiang, C. Shen, Z. Zhan, R. Zou, J. Li, L. Fan, T. Xiao, W. Li, Q. Hua Deng, L. Peng, X. Wang, and W. Wu, "Fabrication of 4.4 THz quantum cascade laser and its demonstration in high-resolution digital holographic imaging," J. Alloys Compd. **771**, 106–110 (2019).
114. M. Humphreys, J. Grant, I. Escorcia-Carranza, C. Accarino, M. Kenney, Y. Shah, K. Rew, and D. Cumming, "Video-rate terahertz digital holographic imaging system," Opt. Express **26**, 25805–25813 (2018).
115. R. J. Mahon, J. A. Murphy, and W. Lanigan, "Digital holography at millimetre wavelengths," Opt. Commun. **260**, 469–473 (2006).
116. C. F. Cull, D. A. Wikner, J. N. Mait, M. Mattheiss, and D. J. Brady, "Millimeter-wave compressive holography," Appl. Opt. **49**, E67–E82 (2010).
117. X. Han, W. Shi, L. Hou, M. Xu, H. Liu, and Y. Xu, "Terahertz off-axis digital holography," in *41st International Conference on Infrared, Millimeter, and Terahertz waves (IRMMW-THz)* (2016), pp. 1–2.
118. A. Tamminen, J. Ala-Laurinaho, and A. V. Raisanen, "Indirect holographic imaging at 310 GHz," in *European Radar Conference* (2008), pp. 168–171.
119. M. S. Heimbeck, M. K. Kim, D. A. Gregory, and H. O. Everitt, "Terahertz digital holography using angular spectrum and dual wavelength reconstruction methods," Opt. Express **19**, 9192–9200 (2011).
120. G. Hislop, L. Li, and A. Hellicar, "Phase retrieval for millimeter-and submillimeter-wave imaging," IEEE Trans. Antennas Propag. **57**, 286–290 (2009).
121. H. Huang, D. Wang, W. Li, L. Rong, Z. D. Taylor, Q. Deng, B. Li, Y. Wang, W. Wu, and S. Panezai, "Continuous-wave terahertz multi-plane in-line digital holography," Opt. Lasers Eng. **94**, 76–81 (2017).
122. Q. Li, S. Ding, Y. Li, K. Xue, and Q. Wang, "Experimental research on resolution improvement in CW THz digital holography," Appl. Phys. B **107**, 103–110 (2012).
123. J. Hu, Q. Li, and S. Cui, "Research on object-plane constraints and hologram expansion in phase retrieval algorithms for continuous-wave terahertz inline digital holography reconstruction," Appl. Opt. **53**, 7112–7119 (2014).
124. J. Hu, Q. Li, and Y. Zhou, "Support-domain constrained phase retrieval algorithms in terahertz in-line digital holography reconstruction of a nonisolated amplitude object," Appl. Opt. **55**, 379–386 (2016).
125. H. Huang, D. Wang, L. Rong, X. Zhou, Z. Li, and Y. Wang, "Application of autofocusing methods in continuous-wave terahertz in-line digital holography," Opt. Commun. **346**, 93–98 (2015).
126. D. Wang, Y. Zhao, L. Rong, M. Wan, X. Shi, Y. Wang, and J. T. Sheridan, "Expanding the field-of-view and profile measurement of covered objects in continuous-wave terahertz reflective digital holography," Opt. Eng. **58**, 023111 (2019).
127. H. Huang, D. Wang, L. Rong, S. Panezai, D. Zhang, P. Qiu, L. Gao, H. Gao, H. Zheng, and Z. Zheng, "Continuous-wave off-axis and in-line terahertz digital holography with phase unwrapping and phase autofocusing," Opt. Commun. **426**, 612–622 (2018).
128. Y. Zhao, J.-F. Vandenrijt, M. Kirkove, and M. P. Georges, "Imaging quality and resolution enhancement by iterative phase retrieval in THz off-axis digital holography," in *Digital Holography and Three-Dimensional Imaging* (Optical Society of America, 2019), paper Th4B-3.
129. J. W. Goodman, *Introduction to Fourier Optics* (Roberts and Company, 2005).
130. J. Rodenburg, A. Hurst, and A. Cullis, "Transmission microscopy without lenses for objects of unlimited size," Ultramicroscopy **107**, 227–231 (2007).
131. D. Gabor, "A new microscopic principle," Nature **161**, 777–778 (1948).
132. U. Schnars and W. Jueptner, *Digital Holography: Digital Hologram Recording, Numerical Reconstruction, and Related Techniques* (Springer, 2005).
133. P. Picart, *New Techniques in Digital Holography* (Wiley, 2015).
134. P. Ferraro, A. Wax, and Z. Zalevsky, *Coherent Light Microscopy: Imaging and Quantitative Phase Analysis* (Springer, 2011), Vol. **46**.
135. P. K. Rastogi and E. Hack, *Optical Methods for Solid Mechanics: A Full-Field Approach* (Wiley, 2012).
136. L. Valzania, *Coherent Lensless Imaging Techniques Using Terahertz Radiation* (University of Bern. Institute of Applied Physics, 2019).
137. M. Takeda, H. Ina, and S. Kobayashi, "Fourier-transform method of fringe-pattern analysis for computer-based topography and interferometry," J. Opt. Soc. Am. **72**, 156–160 (1982).
138. K. Matsushima, H. Schimmel, and F. Wyrowski, "Fast calculation method for optical diffraction on tilted planes by use of the angular spectrum of plane waves," J. Opt. Soc. Am. A **20**, 1755–1762 (2003).
139. K. Matsushima, "Formulation of the rotational transformation of wave fields and their application to digital holography," Appl. Opt. **47**, D110–D116 (2008).
140. R. Mahon, A. Murphy, and W. Lanigan, "Terahertz holographic image reconstruction and analysis," in *Infrared and Millimeter Waves, Conference Digest of the 2004 Joint 29th International Conference and 12th International Conference on Terahertz Electronics* (IEEE, 2004), pp. 749–750.
141. X. Wang, L. Hou, and Y. Zhang, "Continuous-wave terahertz interferometry with multiwavelength phase unwrapping," Appl. Opt. **49**, 5095–5102 (2010).
142. T. Nguyen, J. Valera, and A. Moore, "Optical thickness measurement with multi-wavelength THz interferometry," Opt. Lasers Eng. **61**, 19–22 (2014).
143. R. Bamler and P. Hartl, "Synthetic aperture radar interferometry," Inverse Prob. **14**, R1–R54 (1998).
144. M. Guizar-Sicairos, S. T. Thurman, and J. R. Fienup, "Efficient subpixel image registration algorithms," Opt. Lett. **33**, 156–158 (2008).
145. T. Latychevskaia and H.-W. Fink, "Solution to the twin image problem in holography," Phys. Rev. Lett. **98**, 233901 (2007).
146. G. Koren, F. Polack, and D. Joyeux, "Iterative algorithms for twin-image elimination in in-line holography using finite-support constraints," J. Opt. Soc. Am. A **10**, 423–433 (1993).
147. L. Rong, Y. Li, S. Liu, W. Xiao, F. Pan, and D. Wang, "Iterative solution to twin image problem in in-line digital holography," Opt. Lasers Eng. **51**, 553–559 (2013).
148. K. Xue, Q. Li, Y.-D. Li, and Q. Wang, "Continuous-wave terahertz in-line digital holography," Opt. Lett. **37**, 3228–3230 (2012).
149. Z. Li, L. Li, Y. Qin, G. Li, D. Wang, and X. Zhou, "Resolution and quality enhancement in terahertz in-line holography by sub-pixel sampling with double-distance reconstruction," Opt. Express **24**, 21134–21146 (2016).
150. T. Latychevskaia and H.-W. Fink, "Resolution enhancement in digital holography by self-extrapolation of holograms," Opt. Express **21**, 7726–7733 (2013).
151. G. Chen and Q. Li, "Markov chain Monte Carlo sampling based terahertz holography image denoising," Appl. Opt. **54**, 4345–4351 (2015).
152. J. Miao, D. Sayre, and H. Chapman, "Phase retrieval from the magnitude of the Fourier transforms of nonperiodic objects," J. Opt. Soc. Am. A **15**, 1662–1669 (1998).
153. R. W. Gerchberg, "A practical algorithm for the determination of phase from image and diffraction plane pictures," Optik **35**, 237–246 (1972).

154. G. Pedrini, W. Osten, and Y. Zhang, "Wave-front reconstruction from a sequence of interferograms recorded at different planes," Opt. Lett. **30**, 833–835 (2005).
155. G. Hislop, G. C. James, and A. Hellicar, "Phase retrieval of scattered fields," IEEE Trans. Antennas Propag. **55**, 2332–2341 (2007).
156. P. Almoro, G. Pedrini, and W. Osten, "Complete wavefront reconstruction using sequential intensity measurements of a volume speckle field," Appl. Opt. **45**, 8596–8605 (2006).
157. N. V. Petrov, V. G. Bespalov, and M. V. Volkov, "Phase retrieval of THz radiation using set of 2D spatial intensity measurements with different wavelengths," Proc. SPIE **8281**, 82810J (2012).
158. N. V. Petrov, A. N. Galiaskarov, T. Y. Nikolaeva, and V. G. Bespalov, "The features of optimization of a phase retrieval technique in THz frequency range," Proc. SPIE **8413**, 84131T (2012).
159. L. Valzania, P. Zolliker, and E. Hack, "Coherent terahertz imaging of a textile and a hidden object," in *Digital Holography and Three-Dimensional Imaging* (Optical Society of America, 2019), paper Th4B-2.
160. W. Hoppe, "Diffraction in inhomogeneous primary wave fields. 1. Principle of phase determination from electron diffraction interference," Acta Crystallogr. A **25**, 495–501 (1969).
161. J. M. Rodenburg and H. M. Faulkner, "A phase retrieval algorithm for shifting illumination," Appl. Phys. Lett. **85**, 4795–4797 (2004).
162. P. Thibault, M. Dierolf, A. Menzel, O. Bunk, C. David, and F. Pfeiffer, "High-resolution scanning x-ray diffraction microscopy," Science **321**, 379–382 (2008).
163. P. Thibault, M. Dierolf, O. Bunk, A. Menzel, and F. Pfeiffer, "Probe retrieval in ptychographic coherent diffractive imaging," Ultramicroscopy **109**, 338–343 (2009).
164. A. M. Maiden and J. M. Rodenburg, "An improved ptychographical phase retrieval algorithm for diffractive imaging," Ultramicroscopy **109**, 1256–1262 (2009).
165. P. Thibault and A. Menzel, "Reconstructing state mixtures from diffraction measurements," Nature **494**, 68–71 (2013).
166. A. Maiden, M. Humphry, M. Sarahan, B. Kraus, and J. Rodenburg, "An annealing algorithm to correct positioning errors in ptychography," Ultramicroscopy **120**, 64–72 (2012).
167. F. Pfeiffer, "X-ray ptychography," Nat. Photonics **12**, 9–17 (2018).
168. D. F. Gardner, M. Tanksalvala, E. R. Shanblatt, X. Zhang, B. R. Galloway, C. L. Porter, and R. Karl, Jr., C. Bevis, D. E. Adams, H. C. Kapteyn, M. M. Murnane, and G. F. Mancini, "Subwavelength coherent imaging of periodic samples using a 13.5 nm tabletop high-harmonic light source," Nat. Photonics **11**, 259–263 (2017).
169. O. Bunk, M. Dierolf, S. Kynde, I. Johnson, O. Marti, and F. Pfeiffer, "Influence of the overlap parameter on the convergence of the ptychographical iterative engine," Ultramicroscopy **108**, 481–487 (2008).
170. E. H. Tsai, I. Usov, A. Diaz, A. Menzel, and M. Guizar-Sicairos, "X-ray ptychography with extended depth of field," Opt. Express **24**, 29089–29108 (2016).
171. A. Maiden, D. Johnson, and P. Li, "Further improvements to the ptychographical iterative engine," Optica **4**, 736–745 (2017).
172. L. Valzania, E. Hack, P. Zolliker, R. Brönnimann, and T. Feurer, "Resolution limits of terahertz ptychography," Proc. SPIE **10677**, 1067720 (2018).
173. F. Zhang, I. Peterson, J. Vila-Comamala, A. Diaz, F. Berenguer, R. Bean, B. Chen, A. Menzel, I. K. Robinson, and J. M. Rodenburg, "Translation position determination in ptychographic coherent diffraction imaging," Opt. Express **21**, 13592–13606 (2013).
174. P. Dwivedi, A. Konijnenberg, S. Pereira, and H. Urbach, "An alternative method to correct translation positions in ptychography," Proc. SPIE **10677**, 106772A (2018).
175. F. Blanchard, J. E. Nkeck, D. Matte, R. Nechache, and D. G. Cooke, "A low-cost terahertz camera," Appl. Sci. **9**, 2531 (2019).
176. "Terasense imaging products," 2019, https://bit.ly/2GDqd4A.
177. L. E. Marchese, M. Terroux, D. Dufour, M. Bolduc, C. Chevalier, F. Généreux, H. Jerominek, and A. Bergeron, "Case study of concealed weapons detection at stand-off distances using a compact, large field-of-view THz camera," Proc. SPIE **9083**, 90832G (2014).
178. I. Alexeenko, J.-F. Vandenrijt, G. Pedrini, C. Thizy, B. Vollheim, W. Osten, and M. P. Georges, "Nondestructive testing by using long-wave infrared interferometric techniques with CO_2 lasers and microbolometer arrays," Appl. Opt. **52**, A56–A67 (2013).
179. M. D. Seaberg, B. Zhang, D. F. Gardner, E. R. Shanblatt, M. M. Murnane, H. C. Kapteyn, and D. E. Adams, "Tabletop nanometer extreme ultraviolet imaging in an extended reflection mode using coherent Fresnel ptychography," Optica **1**, 39–44 (2014).
180. A. M. Maiden, M. J. Humphry, and J. Rodenburg, "Ptychographic transmission microscopy in three dimensions using a multi-slice approach," J. Opt. Soc. Am. A **29**, 1606–1614 (2012).
181. R. Horstmeyer, H. Ruan, and C. Yang, "Guidestar-assisted wavefront-shaping methods for focusing light into biological tissue," Nat. Photonics **9**, 563–571 (2015).
182. L.-H. Yeh, L. Tian, and L. Waller, "Structured illumination microscopy with unknown patterns and a statistical prior," Biomed. Opt. Express **8**, 695–711 (2017).
183. A. P. Mosk, A. Lagendijk, G. Lerosey, and M. Fink, "Controlling waves in space and time for imaging and focusing in complex media," Nat. Photonics **6**, 283–292 (2012).